4D Combustion and Flow Diagnostics Based on Tomographic Chemiluminescence and Volumetric Laser Induced Fluorescence

Yue Wu

Dissertation submitted to the faculty of the Virginia Polytechnic Institute and State University in partial fulfillment of the requirements for the degree of

Doctor of Philosophy

In

Aerospace Engineering

Lin Ma, Chair

Kevin T. Lowe

Heng Xiao

Michael K. Philen

November 28th, 2016
Blacksburg, VA

Keywords: Optical diagnostics, Tomography, Laser-induced fluorescence

4D Combustion and Flow Diagnostics Based on Tomographic Chemiluminescence and Volumetric Laser Induced Fluorescence

Yue Wu

Abstract

Turbulent flows and flames are inherently three-dimensional (3D) in space and transient in time. As a result, diagnostic techniques which can provide 4D measurement (4D in this dissertation refers to all three spatial directions and time) have been long desired. The purpose of this dissertation is to investigate two of such diagnostics both for the fundamental study of turbulent flow and combustion processes and also for the applied research of practical devices. These two diagnostics are respectively tomographic chemiluminescence (TC) and volumetric laser induced fluorescence (VLIF). The TC technique uses the chemiluminescence emission from flame radicals to enable 4D measurements in of flame topography at high speed. The VLIF technique uses the LIF transition of a target species to enable 4D measurements or visualization of the key flows and flame parameters. This dissertation describes the numerical and experimental validation of these two techniques, and explores their capabilities and limitations. It is expected that the results obtained in this dissertation lay the groundwork for further development and expanded application of 4D diagnostics for the study of turbulent flows and combustion processes.

4D Combustion and Flow Diagnostics Based on Tomographic Chemiluminescence and Volumetric Laser Induced Fluorescence

Yue Wu

General Audience Abstract

Optical diagnostics have become indispensable tools for the study of turbulent flows and flames. However, optical diagnostics developed in the past have been primarily limited to measurements at a point, along a line, or across a two-dimensional (2D) plane; while turbulent flows and flames are inherently four-dimensional (three-dimensional in space and transient in time). As a result, diagnostic techniques which can provide 4D measurement have been long desired. The purpose of this dissertation is to investigate two of such 4D diagnostics both for the fundamental study of turbulent flow and combustion processes and also for the applied research of practical devices. These two diagnostics are respectively code named tomographic chemiluminescence (TC) and volumetric laser induced fluorescence (VLIF). For the TC technique, the emission of light as the result of combustion (i.e. chemiluminescence) is firstly recorded by multiple cameras placed at different orientations. A numerical algorithm is then applied on the data recorded to reconstruct the 4D flame structure. For the VLIF technique, a laser is used to excite a specific species in the flow or flame. The excited species then de-excite to emit light at a wavelength longer than the laser wavelength. The emitted light is then captured by optical sensors and again, the numerical algorithm is applied to reconstruct the flow or flame structure. This dissertation describes the numerical and experimental validation of these two techniques, and explores their capabilities and limitations. It is expected that the results obtained in this dissertation lay the groundwork for further development and expanded application of 4D diagnostics for the study of turbulent flows and combustion processes.

Acknowledgement

I would not have had accomplished this doctoral dissertation and my Ph.D study in Virginia Tech without the help and support from the people around me. I would like to take this opportunity to thank all of you who have contributed to my academic and personal life in Blacksburg for the past three years. It is important for me to first and foremost acknowledge Dr. Lin Ma, as an advisor, professor, mentor and friend. Dr. Ma has provided me immeasurable help and taught me how to perform professionally in all aspects of engineering. He set up a model of an outstanding researcher, inspired me to get close to the model, and really brought my work into a different level. I also would like to thank Dr. Todd Lowe, Dr. Heng Xiao and Dr. Michael Philen for serving on my advisory committee and providing me professional and academic advice.

Another sincere acknowledgement is in order for my colleagues in Virginia Tech for sharing the unforgettable memories with me. In particular, on individual stands above the rest: Qingchun Lei. We came to the campus together in 2013 and he was always there for me every step of the way with advice and research help. When my research stuck at some points, the discussion between the two of us can always help me make a progress. More important to me, Qingchun and his family brought me to the community and enjoy the after-research life together. I do not think I would have survived to this day without him and his family. Also, to the many other students who helped me make this possible. Dr. Xuesong Li, Dr. A.J. Wickersham, Dr. Fan He, MinWook Kang, Wenjiang Xu, Haoting Wang, Ning Liu, Yihua Ren, Tyler Capil, Jordan Ikeda and many others, thank you very much for having the patience with me on research projects and for shaking me out of the monotony when I really need it.

I cannot forget to give my great gratitude to my families, for their love and supports which has always been leading and encouraging me for more than twenty years. I really hope all of you

maintain a healthy body and wonderful life. To my Mom and Dad, although I may still need some time to fully “grow up” as a man, I will keep pushing myself and let you proud just as how I did in the past years. Best wishes to two of you.

Lastly and specially, I would like to thank all guys from the internet friend circle. It was so nice to meet and chat with all of you guys. We shared the same hobby as a part-time singer or a game player. Even though we barely have a chance to meet offline, you guys still built up my spare time during the past three years. I would like to share more time with you, so hope all of us can keep “showing up” online, even after we graduating, starting working, getting married (hopefully for me…). And finally, the world is held in our hands, El Psy Congroo.

Table of Contents

List of Figures

List of Tables

Chapter 1 Introduction

1.1 Overview of optical diagnostics

Non-intrusive optical diagnostics have been demonstrated as powerful tools for the study of the flow and combustion processes[1]. Compared to traditional intrusive diagnostic methods (e.g. Pitot tubes, hotwire and thermocouple), optical diagnostics avoid physical contact with the target flow field. Thus, optical diagnostics remove the disturbance to the target flow and can endure harsh measurement environments such as high temperature, high pressure, explosive and corrosive species. Furthermore, optical diagnostics also provide a new perspective for remote control thanks to the availability of high-performance optical component such as high speed lasers, cameras, and fibers.

A suite of optical diagnostic techniques has been researched and developed in the past decades for flow and combustion research. As an incomplete list, optical diagnostic techniques developed and relatively matured in the past include passive techniques (which does not require the use of an external source to excite the target flow or flame) such as chemiluminescence [2], soot radiation [3, 4] and surface radiation [5, 6]; and laser-based analysis techniques such as Particle Image Velocimetry (PIV) [7, 8], Laser Doppler Anemometry (LDA) [9, 10], Phase Doppler Anemometry (PDA) [11, 12], Laser-Induced Fluorescence (LIF) [13-15], Laser Induced Incandescence (LII) [16, 17], Raman scattering [18, 19], Rayleigh scattering [20, 21], Mie scattering [22, 23], and light absorption techniques [24, 25]. These techniques are based on different physics (e.g. emission, excitation, scattering, refraction, etc.) and they are applied in practical measurements to measure different flow parameters, ranging from temperature, velocity, chemical species concentration, mixture fraction, etc. Note that no single technique is capable of measuring all flow parameters of interests in a typical experiment, thus multiple different techniques are usually combined by

researchers to measure the properties of interests simultaneously in order to achieve a more complete analysis of the flow or combustion system.

Before moving on to the specific optical diagnostic technique studied in this dissertation, it is worthwhile to point out some of the limitations and complications of optical diagnostic measurements. First and foremost, optical access is always a major concern in the practical application of optical diagnostics. Practical devices usually have limited optical access. For instance, the test section of wind/water tunnels usually have observation windows with limited physical dimension, and the combustion chamber of most engines are manufactured using opaque materials (e.g. metals, ceramics, etc.). Therefore, it is not trivial to overcome the practical constraints and obtain enough optical access to implement the intended optical diagnostic. Second, the quantitative interpretation of optical signal is not always straightforward or even feasible. Understanding the translation from the optical signal to the target flow/flame properties can involve complicated spectroscopic analysis and not all the parameters required in such analysis are readily available. Third, the cost of optical sensors (e.g. cameras, lenses and lasers) can be relatively expensive compared with other measurement techniques. Plenty of past efforts have been invested to overcome these limitations and complications, and these efforts will surely evolve together with the advancement of laser, fiber, camera, and optic technologies. For example, fibers [26, 27] and fiber-based endoscopes (FBEs) [28, 29] have been shown to be effective in gather the maximum amount of information with minimal optical access because of their relatively small footprint (compared to cameras) and their ability to circumvent the need for line-of-sight optical access [30]. Also, researchers have been continuing the development of spectroscopic databases and computational algorithms with high efficiency to interpret the optical signal to obtain the target properties [31-33], and these database and algorithms have been and are still being validated [34].

1.2 Development of 4D diagnostics

This work defines dimensionality based both on space and time, and 4D diagnostics refer to diagnostics that can resolve the target property with both adequate temporal resolution and spatial resolution in all three spatial directions. Following this definition of terminology, a 3D diagnostic technique refers to a technique can either resolve a target parameter in all three dimensions of space but without temporal resolution, or in two dimensions of space (i.e. a planar measurement) and time.

It is also necessary to clarify the definition of measurement duration and the repetition rate of measurements used in this work. This work refers to “single-shot” measurement as measurements that were accomplished during the duration of one single laser pulse (pulsed lasers are typically used as the light source in many of the optical diagnostics), which ranged from a few nanoseconds to a few hundred nanoseconds in this work. Such single-shot measurements are sufficiently short to freeze any motion of the target flow of practical concern.

This work refers to high-speed or high-repetition rate measurements in terms of the temporal separation between two consecutive measurements. For example, if a series of measurements were obtained and the temporal separation between any two consecutive measurements is 1 ms, then the measurement will be referred to as measurements at a repetition rate of 1 kHz (or simply 1 kHz measurements). Moreover, if each of the measurement in the series is made within the duration of a single laser pulse, then these measurements will be referred to as single-shot measurements at 1 kHz.

With the above definition of dimensionality, measurement duration, and measurement rate, here we briefly overview the possibility strategies to obtained 4D single-shot measurements via optical diagnostics. With currently available optical sensors and image equipment, two potential

approaches have attracted the majority of research attention to enable 4D measurements: the rapid scanning of 2D planar techniques [35, 36] and tomography [37, 38]. The first approach extends a 2D planar technique to 4D measurements by rapidly scanning the illumination laser sheet sequentially across multiple spatial locations. When the time scale required for scanning is small relative to the flow time scale, the 2D measurements obtained sequentially at multiple locations can be stacked together for forming a 4D measurement. At least conceptually, any 2D planar techniques can be extended by this approach to obtain 4D measurements. For example, based on this method, past efforts have demonstrated the 4D measurement of chemical species concentration based on planar laser induced fluorescence (PLIF) [39, 40], 4D measurement of soot volume fraction based on laser induced incandescence [41], and 4D visualization of flow-structure-based planar Mie scattering [35].

In contrast to the first scanning approach, the second approach is based on tomography and it obtains instantaneous 4D measurements without scanning. This approach obtains 4D measurements by measuring multiple projections of the target flow/flame from various locations and orientations simultaneously, and then by performing a tomographic inversion using the projections as inputs. Multiple-dimensional optical diagnostics developed in the past based on the tomographic approach include tunable diode laser absorption spectroscopy (TDLAS) [42, 43] and hyperspectral absorption tomography (HT) [44, 45] to resolve the distribution of chemical species and temperature, tomographic PIV [8] to resolve velocity field, tomographic Mie scattering [46] and tomographic chemiluminescence (TC) [47, 48] to resolve turbulent flame fronts. Compared with the first approach based on scanning, the tomographic approach obtains 4D measurements instantaneously and volumetrically without scanning, resulting in several fundamental differences between these two approaches. In terms of the measurement repetition, the first approach is limited

typically by the time required to scan and the repletion rate of the illumination laser, whereas the second approach is limited by the frame rate of the camera to capture the projections or by the repetition rate of the lasers (both of which can reach tens of kHz with commercially available products). In terms of spatial resolution, the first approach enjoys well-defined spatial resolution in the plane of the illumination laser sheet. However, the spatial resolution in the direction of the scan depends on several factors, including the step size of the scan, the thickness of the laser sheet, and the accuracy and reproducibility of the scan. The spatial resolution of the tomographic approach, in contrast, depends on the imaging optics and the inversion algorithm in all three directions [49].

This dissertation focuses on the development and validation of two 4D techniques based on the tomographic approach. The first technique is the tomographic chemiluminescence (TC) technique, and the second one is the volumetric laser induced fluorescence (VLIF) technique. The motivation and goal of studying TC and VLIF in this dissertation are twofold. First, for the TC technique, past work has conducted extensively numerical validations, but experimental validations have been limited either to simple flames or indirect comparisons for turbulent flames. Therefore, the first goal of this work is to design an experiment that can directly validate the TC technique in turbulent flames. To accomplish this goal, this work designed an experiment in which the TC technique was simultaneously performed with an established PLIF measurements, such that the 3D measurements obtained from the TC technique can be directly compared to and validated by the PLIF measurements. Second, the TC technique has intrinsic limitations and restrictions, and an alternative method, the VLIF method, is thus explored to overcome these limitations. The TC approach relies on the nascent emissions from excited radicals generated by chemical reactions, such as CH* and/or OH*. Therefore the signal intensity of chemiluminescence

is relatively low (compared with signal generated by laser-based approaches). When TC measurements are desired at high repetition rate, the exposure time (i.e., the measurement duration) will decrease and so does the signal-to-noise ratio (SNR) of the measurements. Moreover, if we would like to study the distribution of a particular radical (such as CH*) in the flow or flame, additional optical filters will be needed to block the chemiluminescence signal from other radicals, which further reduces the signal level and SNR. To overcome these limitations and restrictions, a new approach, VLIF, is developed. The VLIF approach combined LIF with computed tomography to obtain 4D measurements. More specifically, the VLIF approach uses a thick laser slab (in contrast to the thin laser sheet used in static PLIF or scanning PLIF) to excite the target radicals volumetrically and continuously. The LIF signals emitted by the target radicals are then measured from multiple perspectives to form projections, and a tomographic inversion is applied. Compared with TC, the VLIF technique enable three advantages in resolving the flow/flame topography to overcome the limitations of the TC technique. First, the LIF signal can be significantly stronger than the nascent chemiluminescence emissions, which helps to improve the SNR of the measurements. Second, with a careful choice of the excitation laser, the LIF signal is species specific, i.e., the signal is only generated from CH or OH [50]. Third, the measurement duration of LIF measurement is determined by the duration of the laser pulse (which ranged from several nanoseconds to several hundreds of nanoseconds), which is significantly shorter than the exposure time used in the TC measurements. As a result, the LIF-based 4D diagnostics can be applied to (i.e., to “freeze”) more transient flows than the TC technique.

1.3 Organization and summary of contributions

The rest of this dissertation is organized as follows. Chapter 2 discusses the experimental validation of TC in highly turbulent flame. The focus is to directly and quantitatively validate the TC result of flame topography by comparing it against simultaneous planar measurements obtained from established PLIF technique. Since PLIF is a planar technique, the comparison was performed by overlapping the PLIF image of the flame front on 2D reconstructed slices of TC. Such comparison also illustrates the capability and limitation of both techniques. It can be concluded from the comparison that the TC technique enables more total imaging elements within a 3D volume and provides information unachievable from 2D measurements (e.g. Gaussian curvature of the flame front in 3D)

After the validation measurements in chapter 2, chapter 3 demonstrates the 4D TC measurement on a highly turbulent flame to obtain 4D flame properties, including the location of the flame front and flame curvatures. For the flame front location analysis, the PDF of flame front is extracted from a number of reconstructions of the 4D measurement, and the PDFs of the flame at different spatial locations are compared to achieve an understanding of the turbulent flame topography statistically. For the flame front curvature analysis, 2D curvatures along specific directions and 3D curvature under various definition are calculated from the reconstructed flame front. The PDFs of 2D and 3D curvatures are also compared to quantify the flame surface in 3D. These 4D measurements and statistics provide a valuable database for the validation and development of combustion models.

With the understanding accumulated from the study in chapters 2 and 3 on the capabilities and limitations of the TC technique, chapters 4 and 5 report the development of the VLIF technique to overcome the limitations of the TC technique.

Chapter 4 is aimed to overcome the intrinsic limitation of TC in signal separation process. Unlike TC measurements presented in chapter 2 and 3 that record the chemiluminescence signal, which may be emitted by several chemical species, chapter 4 reports the development of a VLIF technique that can only target the signal from one single chemical species. More specifically, chapter 4 describes a single-shot VLIF measurement of iodine vapor, seeded in turbulent flows as a flow tracer. The iodine vapor is excited by a thick laser slab volumetrically and the LIF signal is recorded by multiple cameras from different perspectives. Band-pass filters were applied to block possible scattering and reflection to ensure that signals recorded are fluorescence signals from iodine only. Then 3D reconstructions of iodine concentration are performed to study the topography of the turbulent jet flow. By comparing projections and reconstructions obtained using VLIF and TC, respectively, the superiority of the VLIF technique is clarified.

Chapter 5 focuses on overcoming the repetition rate and signal level issues of TC by demonstrating VLIF measurements up to 10 kHz. As mentioned earlier, the application of TC involves a tradeoff between repetition rate and signal level: higher repetition rate requires shorter exposure time of the camera, resulting in lower signal level. With LIF-based measurements, the measurement duration is limited by the duration of the laser pulse (on the order a few to several hundreds of nanoseconds), not the exposure time of the cameras. Therefore the repetition rate and signal level of LIF-based technique depend on the repetition and pulse energy of the laser, no longer on the exposure time of the camera and therefore can be controlled independently. The results demonstrated VLIF measurements based on iodine vapor up to 10 kHz with good signal level, and the VLIF signal level and its impact on the reconstruction accuracy are studied by performing measurements under different repetition rates. Furthermore, a simulation study using a two-level LIF model was performed in parallel to under the fundamentals of the VLIF technique.

These results suggest that the VLIF technique can achieve even higher repletion rate and high signal level than reported in this work with the availability of more powerful lasers.

Finally, chapter 6 concludes the dissertation and suggest some possible directions for future work.

The contribution of this dissertation to the flow diagnostic community can be summarized as follows:

1) A TC technique was developed, validated, and demonstrated in the dissertation to quantitatively resolve the temporal dynamics and 3D spatial structures of highly turbulent flames with sub-millimeter spatial resolution and sub-millisecond temporal resolution, greatly extending the diagnostics capabilities for turbulent flames.
2) The TC technique enabled the first piece of 3D data of a representative “envelope flame” and the data included 3D flame topography and 3D flame curvature. Such data is expected to provide new information for the development and validation of turbulent flame models.
3) A VLIF technique was first proposed, validated, and successfully demonstrated to extend LIF-based diagnostics into 4D measurements. The VLIF technique is capable of resolving the distribution of specific chemical species (e.g. iodine molecule in this dissertation) with temporal resolution up to 10 kHz (limited only by the availability of the excitation laser) and sub-millimeter spatial resolution in all three directions.

Chapter 2 Development and Validation of Tomographic Chemiluminescence

2.1 Introduction

Many open questions still exist in our understanding of the complicated processes involved in turbulent combustion [51]. One of the key hurdles to answering such questions is the lack of experimental techniques that can directly measure key flame properties, which are inherently three-dimensional (3D) in space and transient in time. The distribution of the flame front represents one such key property. Many characteristics of turbulent combustion, such as the flame-front location, curvature, and thickness, are directly derived from flame-front measurements. As a result, extensive efforts have been invested to develop techniques to characterize the flame front with adequate spatial and temporal resolutions [37, 52, 53].

Diagnostics based on PLIF [1, 14, 54, 55] and chemiluminescence [37, 38] represent two of the relatively well-established and extensively applied techniques. Diagnostics based on PLIF provide a 2D image of the flame front by using a radical such as CH and OH as a flame marker [55]. The target radical is excited by a thin laser sheet, usually generated by a pulsed laser. The thickness of the laser sheet defines the spatial resolution of the 2D measurements in the depth direction, and the duration of the laser pulse defines the temporal resolution. However, PLIF provides only a 2D image of the 3D reaction-zone structure (on the plane illuminated by the laser sheet), and certain assumptions need to be invoked in order to infer many key parameters of interest (such as curvature, flame surface area, and volume) from the PLIF images [56].

The chemiluminescence approach relies on excited radicals generated by chemical reactions, such as CH* and/or OH*. The nascent emission from these excited radicals provides the signal, therefore eliminating the need for laser illumination and simplifying the experiments. However, reliance on the flame emission causes ambiguities in the measurement spatial resolution because

the image formed on a camera is the result of nascent emission integrated along its line-of-sight. Past work has demonstrated that tomographic chemiluminescence (TC) represents an effective way of overcoming this limitation and enabling spatially-resolved flame-front measurements based on chemiluminescence. The TC approach involves using multiple cameras to image the target flame from multiple orientations. The line-of-sight integrated emission images captured by these cameras (termed projections) are then used as inputs in a tomographic algorithm to reconstruct the 3D flame structures.

Thus, the goal of this chapter was to report the development of the TC diagnostics and its validation by comparing 3D TC against single-shot PLIF measurements. The specific objectives of such comparison are twofold. The first objective was to provide a validation of the 3D TC measurements. The measurement capability has been validated in the past via the use of controlled flames [2, 30] and numerical simulations [37, 49]. A simultaneous PLIF and TC measurement provides another validation of the TC technique via a direct comparison of the 2D PLIF image against a cross-section of the 3D TC measurements. The second objective was to compare the flame structure and properties measured by the PLIF and TC techniques to illustrate the capabilities and limitations of each technique. As a particular example, the flame-front curvature inferred from the 2D PLIF images was compared with that inferred from the 3D TC measurements. Furthermore, it is of both scientific and practical interests to compare chemiluminescence and CH PLIF measurements since they are both widely practiced while they are based on different quantities. However, to our knowledge, their direct comparison has not been feasible thus far because one is a line-of-sight integrated technique and the other a planar technique. Thus the second objective of this chapter was aimed at overcoming this limitation and enabling such a direct comparison.

2.2 Experimental Arrangement

The experimental setup is illustrated schematically in Figure 2-1. Measurements were performed on a rectangular Bunsen burner, the representative "envelope flame" (in which all the reactants must pass through the flame [51]) on which extensive measurements have been performed [52, 57-59]. Measurements on this flame have been performed to characterize its velocity fields using low-and high-speed PIV [59], flame front topography using PLIF [52], and the subsequent inference of other properties such as stretch rate, flame surface density, and burning velocities [52, 57, 58]. However, due to the planar nature of the PLIF and PIV, only 2D data are available on this flame. It is a goal of this chapter to provide the first piece of 3D data of this representative flame. The burner consisted of three parts (labeled as part I, II, and III in Figure 2-1). The central part (part II), with a width (W) of 25.4 mm and a length (L) of 50.8 mm, generated the target flame. A turbulence-generating grid was installed inside part II to wrinkle the target flame. The two parts on the side (parts I and III) generated the pilot flames to stabilize the target flame. The burner was operated with premixed methane and air at an equivalence ratio of 1.07 and a bulk velocity of 5 m/s. Under these conditions, the target flame was about 100 mm in height. The turbulent Reynolds number based on the integral scale was measured (by hot wire anemometry) to be 2,400 in the central region of the burner. At a height 4 mm above the burner exit, the Taylor micro-scale was measured to be about 0.9 mm, also in the central region of the burner. Based on previous measurements [60], the mean stain rate of the flames generated by this burner was ~1000 s^{-1}, with an oscillating frequency in the range of 5 - 10 kHz which approximately corresponded to the inverse of the convection time of integral-scale eddies across the flame surface. However, the flame chemistry and diffusion processes did not display large variations with the rapidly varying strain field. Based on the burner configuration, a Cartesian coordinate

system was defined such that the exit plane of the burner was the *x*-*y* plane, and the *z* axis was defined along the flow direction (i.e., the height direction). The origin was defined as the center point of the exit plane, the *x* axis the central line along the width direction, and the *y* axis the central line along the length direction.

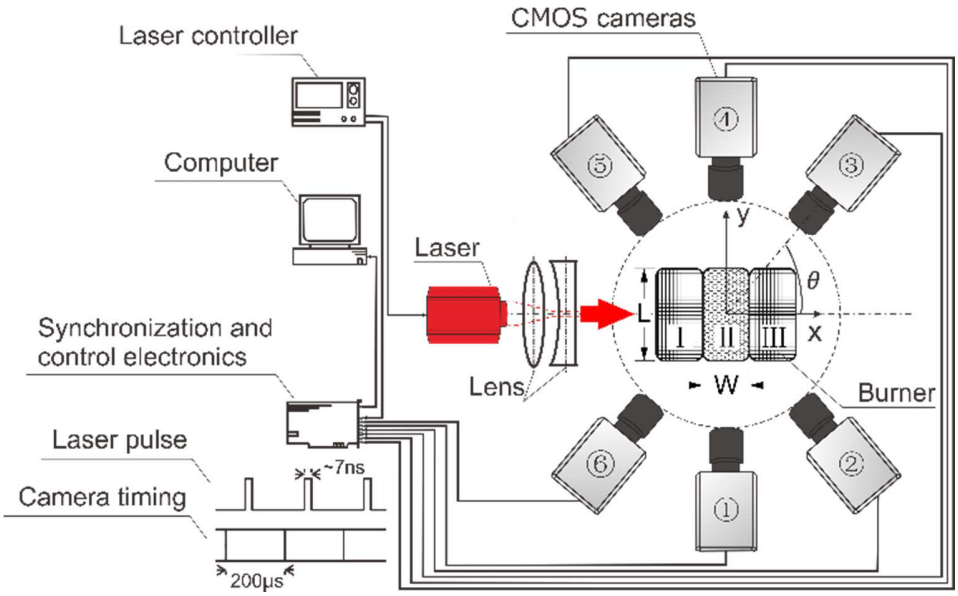

Figure 2-1. Experimental setup.

As shown in Figure 2-1, the setup used a total of 6 CMOS cameras (2 Photron SA-4, 2 Photron SA-5, and 2 Photron SA-Z cameras) to obtain simultaneous PLIF and TC measurements on the target flame. All cameras were aligned in the *x*-*y* plane so that their orientations were specified by θ, defined as the angle formed by the optical axis of a camera relative to the positive *x* direction as shown in Figure 2-1. The focal length and *f*-number of the lenses used on camera 1 through 6 were, respectively, 45 mm and 1.8, 60 mm and 2.8, 50 mm and 1.2; 85 mm and 1.8, 50 mm and 1.2, and 58 mm and 1.2. A pulsed laser (a Sirah CREDO pumped by an Edgewave Nd:YAG) was used to excite the CH as detailed in [61]. The excitation laser pulses were focused to a sheet with a thickness of ~0.3 mm and propagated along the *x* direction through the central plane of the flame. Camera 1, aligned perpendicular to the laser sheet (i.e., with $\theta = 270^{o}$) and equipped with an

intensifier (LaVision HS-IRO), was used to capture the PLIF images. Camera 2 through 6 were used to capture projections of chemiluminescence at θ = 305.7°, 50.1°, 90.4°, 134.5° and 227.1°, respectively, determined through a view registration process as detailed in [28]. The distance from camera 1 through 6 to the flame center were approximately 165.1 mm, 203.2 mm, 165.1 mm, 241.3 mm, 152.4 mm, 152.4 mm, respectively. The placement of the cameras was designed based both on scientific and practical considerations. The scientific considerations included obtaining the most independent information on all the cameras available, and the practical considerations included optical access and physical space available. For example, we expect the reconstruction quality to be improved if an additional camera can be placed above the flame to capture a projection from the top view. The chemiluminescence cameras were used without optical filters for the consideration of signal level and temporal resolution. Thus, the chemiluminescence measurements did not discriminate CH^* chemiluminescence from that of other excited-state species (though the signal was primarily due to CH* in the visible range, as the cameras do not have sensitivity in the UV range). Note that camera 4 was intentionally aligned to be opposite of the PLIF camera (i.e., also perpendicular to the PLIF laser sheet) to facilitate comparison. The operation of the laser and cameras was synchronized in the following way. The laser operated at a repetition rate of 5 kHz (with a laser pulse duration of about 10 ns), and all six cameras were synchronized with the laser with a frame rate of 5 kHz and an exposure time of 200 μs; the effective exposure time for the PLIF measurement was ~10 ns, determined by the laser pulse duration (the intensifier gate time was set to 150 ns). The laser firing was synchronized at the beginning of the exposure time of the cameras.

Figure 2-2 shows a sample set of images measured by all the cameras. Figure 2-2(a) shows the PLIF image captured by camera 1 and Figure 2-2(b) - 2(f) the corresponding chemiluminescence

projections captured by cameras 2 through 6. These images were at different pixel resolution due to the different specifications of each camera. Also a threshold was applied to the images shown in Figure 2-2 to reduce the background and facilitate the comparison. The thresholding value was chosen to differentiate against signals considered to be background/noise and to preserve the flame features. In this chapter, the value was determined to be approximately 21% of the maximum intensity of the raw projections, and the images processed by the thresholding method were used in the subsequent tomographic reconstruction. That is, pixels intensity values below 21% of the peak intensity (for each camera) were set to zero. The thresholding value was estimated by analyzing the raw measured projections in the following three steps: 1) signals in regions where no flame appeared to exist were recorded, 2) the maximum flame intensity on the measured projections was determined, and 3) the ratio between steps 1 and 2 was used as the thresholding value. There was ambiguity and image-to-image variation in both steps 1 and 2. However, the images after thresholding did not vary significantly based on visual examination when the thresholding value changed in a small range. At a frame rate of 5 kHz, the resolution of these images was 1024 × 1024 pixels on cameras 1, 2 and 4, and 864 × 864 pixels on cameras 3, 5 and 6.

The PLIF and TC measurements also had different fields of view (FOV), as illustrated in Figure 2-2(d). The FOV of the PLIF measurements was determined by the height of laser sheet (which was 44 mm in this chapter) and is illustrated by the square with dashed lines as shown in Figure 2-2(d). The FOV of the TC measurements was designed to be ~100 mm to capture the entire flame as shown in Figure 2-2(b) - 2(f), resulting in a measurement volume of 100 mm × 100 mm × 100 mm. Tomographic reconstruction in this entire measurement volume was performed. However, only results from a region ~50.5 × 50.5 × 50.5 mm^3 (as illustrated by the square with solid lines)

are shown for the clarity of comparison with the PLIF measurements. These results in Figure 2-2 also elucidate the overall structure of the Bunsen flame, which consists of two "branches" stabilized on each side of the burner.

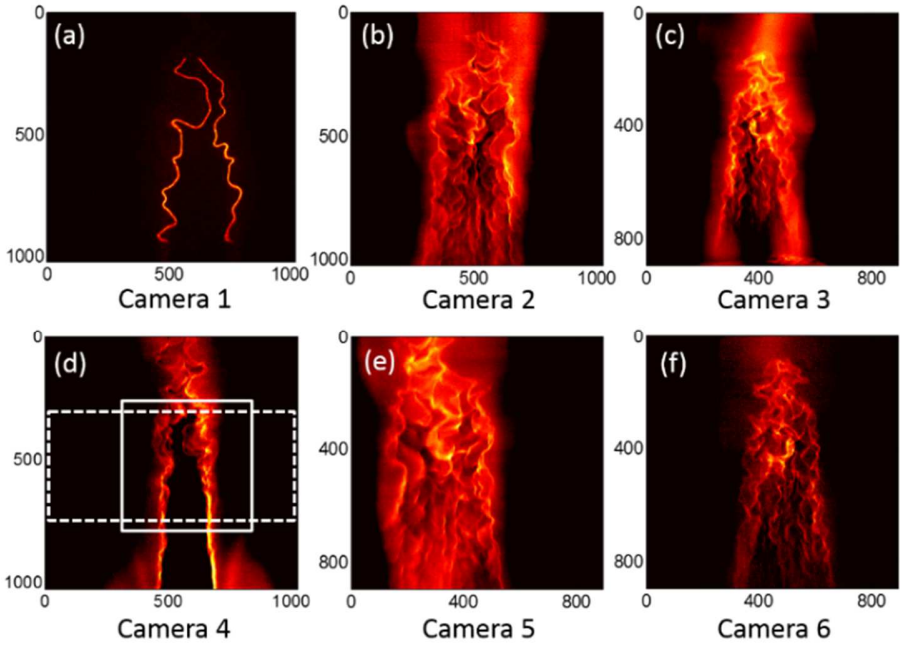

Figure 2-2. A set of flame images taken by 6 cameras simultaneously. Panel (a): the PLIF image. Panel (b)-(f): the chemiluminescence projections from different perspectives.

To further illustrate the nature of the PLIF and TC measurements, Figure 2-3 examines the PLIF and TC measurements more closely by comparing the images obtained on cameras 1 and 4. As mentioned earlier, these two cameras were aligned opposite of each other. Figure 2-3(a) shows the flame front extracted from the PLIF image in Figure 2-3(a) by an edge detection algorithm based on thresholding [62] of signal values. The flame front obtained in Figure 2-3(a) was flipped horizontally (because cameras 1 and 4 were aligned opposite of each other) and overlapped with the TC projection captured by camera 4, as shown in Figure 2-3(b). This figure clearly displays several key aspects of the PLIF and TC measurements (or chemiluminescence measurements in general). First, this comparison illustrates the limitations of both techniques. As seen, the flame

front extracted from the PLIF and the chemiluminescence image agrees only on an overall level, because i) the PLIF image only captured the 3D flame structure across one plane and ii) the chemiluminescence image was line-of-sight integrated. Second, this comparison also illustrates that PLIF can resolve sharp features better than chemiluminescence imaging simply because of the shorter exposure time provided by a Q-switched laser.

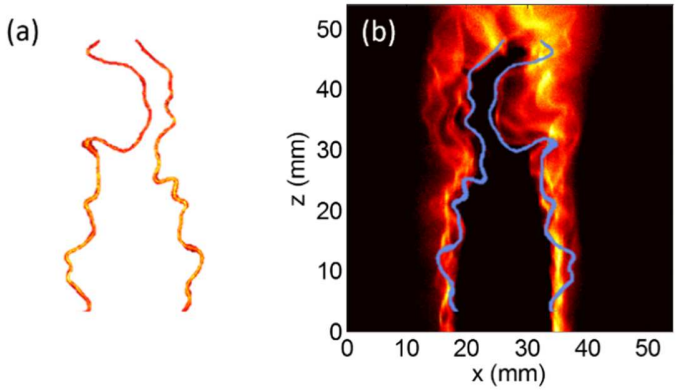

Figure 2-3. Panel (a): Flame front extracted from PLIF projection. Panel (b): Flame front extracted from PLIF overlapped with chemiluminescence projection.

2.3 Tomographic Reconstruction of TC

Projections shown in Figure 2-2(b) - 2(f) were used as inputs to a tomographic reconstruction algorithm to obtain the 3D distributions of the chemiluminescence, which were then used to infer the flame-front locations and calculate other flame properties such as curvature. The tomographic algorithm has been detailed and validated in our previous publications, and only a brief summary is provided here to facilitate the discussion. After discretizing the measurement volume into a series of Cartesian voxels, the projection measured by a camera (denoted as *P*) is related to the desired distribution of the chemiluminescence emissions (denoted as *F*) via the point spread function (*PSF*) as shown below [63]:

$$P(x_P, y_P) = \sum_{x_i=1}^{I} \sum_{y_j=1}^{J} \sum_{z_k=1}^{K} F(x_i, y_j, z_k) \cdot PSF(x_i, y_j, z_k; x_P, y_P) \tag{2-1}$$

where $P(x_P, y_P)$ represents the value of the projection at a pixel located at (x_P, y_P); x_i, y_j, and z_k the indices of the voxels in the x, y, and z directions, respectively; I, J, and K the total number of voxels in each direction; *PSF* the point spread function defined as the projection formed at (x_P, y_P) by a point source located at (x_i, y_j, z_k) with unity intensity. The *PSF* does not depend on F, but it depends on the lens used in the imaging system and the location and orientation of the imaging system. Physically, Eq. (2-1) states that the projection of F on pixel (x_P, y_P) is a weighted summation of signals contributed from all voxels on this pixel, and the weighting factor is the *PSF*. In our algorithm, the *PSF* was calculated by a combination of geometrical ray-tracing [47, 64] and Monte Carlo simulation [65, 66] using the specification of the lenses, and the orientation and location of the cameras as inputs. After the *PSF* for each camera was obtained, Eq. (2-1) was solved for F using the measured Ps as inputs. The algorithm we used to solve Eq. (2-1) was a modified variation of the Algebraic Reconstruction Technique (ART) [37, 47, 49] and a simulated annealing algorithm [32]. This tomographic approach has been validated via numerical simulations [47, 48] and controlled experiments in both non-reacting [22] and reacting flows [47, 48]. The tomography algorithm analyzes how many photons are collected on a given pixel and where these photons are emitted from the measurement volume. The tomography algorithm did not rely on assumptions of parallel beam or in-focus imaging (which have limited validity in practice especially for any extended measurement volume). As a result, it is not required for the entire measurement volume to be within the focal depth of the cameras. Figure 2-4 shows a rendering of a sample based on the projections shown in Figure 2-2. The data shown in Figure 2-4 contains a total of 128 × 128 × 128 voxels (i.e., ~2×10^6 voxels) in a volume of 50.5 × 50.5 × 50.5 mm^3, resulting in a nominal spatial resolution of 0.39 mm.

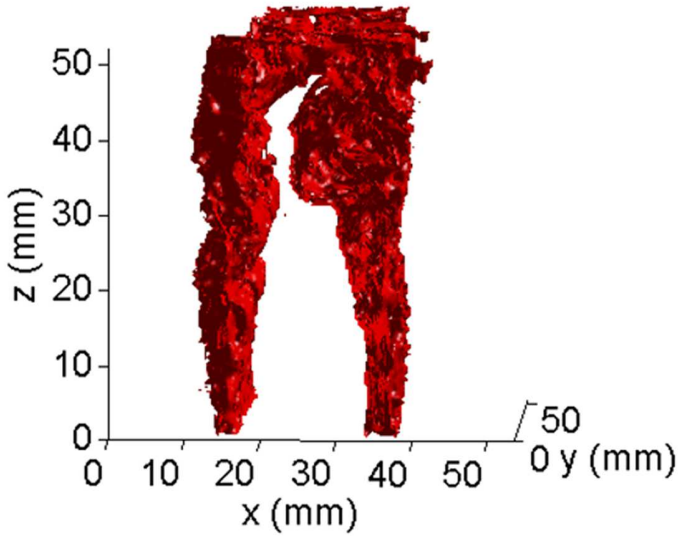

Figure 2-4. 3D rendering of the flame reconstruction.

Figure 2-5 examines the 3D reconstruction more closely. Figure 2-5(a) shows the reconstruction at three different planar locations, and Figure 2-5(b) shows the reconstruction at the central plane of the flame, i.e., on the same plane as the PLIF measurements. Figure 2-5(c) overlaps the flame edge extracted from the PLIF image on top of the reconstruction shown in Figure 2-5(b). As can be seen from Figure 2-5(c), the flame front extracted from the 3D TC measurements matches the PLIF significantly better than the image in Figure 2-5(b), while there are also disagreements (e.g., between points 1 and 1', and 2 and 2'), which were mostly due to two factors. First, the flame front inferred from the PLIF image (which is based on CH) is inherently different from that inferred from TC (which was defined based on chemiluminescence emissions). To minimize the effects of emission contributed from other species such as CO*, this chapter extracted the inner flame edges from the 3D reconstructions to separate the chemiluminescence emissions caused by CH* from those caused by combustion products. Second, as mentioned earlier, the PLIF measurement duration was ~10 ns (during which the flame was essentially frozen), while that for the TC was 0.2 ms. At the bulk velocity of 5 m/s, the 0.2 ms exposure time causes a blurring of 1

mm with our imaging optics, on the same order as the Taylor micro-scale mentioned before. The 1-mm blurring should represent an upper limit of the blurring caused by the exposure time of the TC measurement. For example, the blurring should be less in the horizontal and depth directions. Moreover, the synchronization step between the laser and the cameras (i.e. the temporal location of the laser firing during the exposure time of cameras) could result in a maximum position disagreement of 1 mm (~2% of the overall height) of the PLIF image. Our ongoing work to resolve these issues involves the use of intensified cameras to shorten the exposure time of the TC measurements, and 3D imaging of flame front by volumetric LIF. Note that the 0.39-mm thickness of the voxels was also larger than the thickness of the laser sheet by about 0.09 mm, which could also contribute to the disagreement observed here. However, we expect such disagreement to be relatively minor compared to the two sources discussed above. Despite these issues, the results shown here illustrate the ability to overcome the line-of-sight limitation of chemiluminescence imaging and to resolve the three-dimensionality of turbulent flames with reasonable fidelity. Figure 2-6 shows the comparison between the TC and PLIF measurements at two other instances randomly chosen to show the consistent level of agreement.

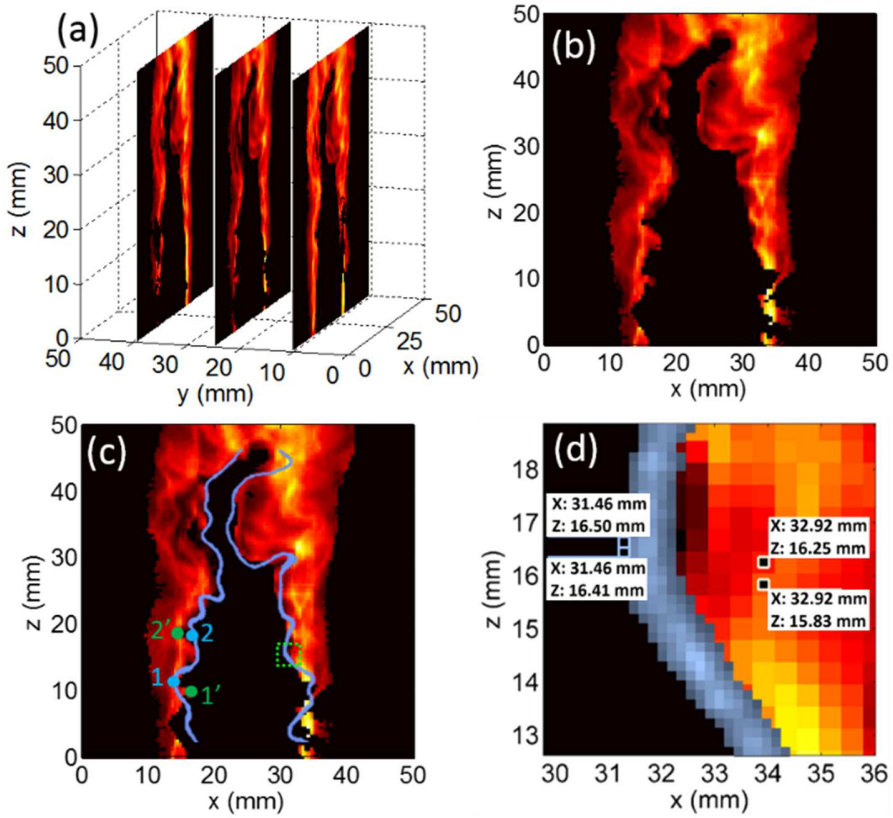

Figure 2-5. Panel (a): three 2D slices of the 3D reconstructed flame structure. Panel (b): central slice of the 3D reconstruction. Panel (c): flame front extracted from PLIF overlapped on the central slice of the 3D reconstruction. Panel (d): closer view of the region in dashed box to show the difference in spatial resolution.

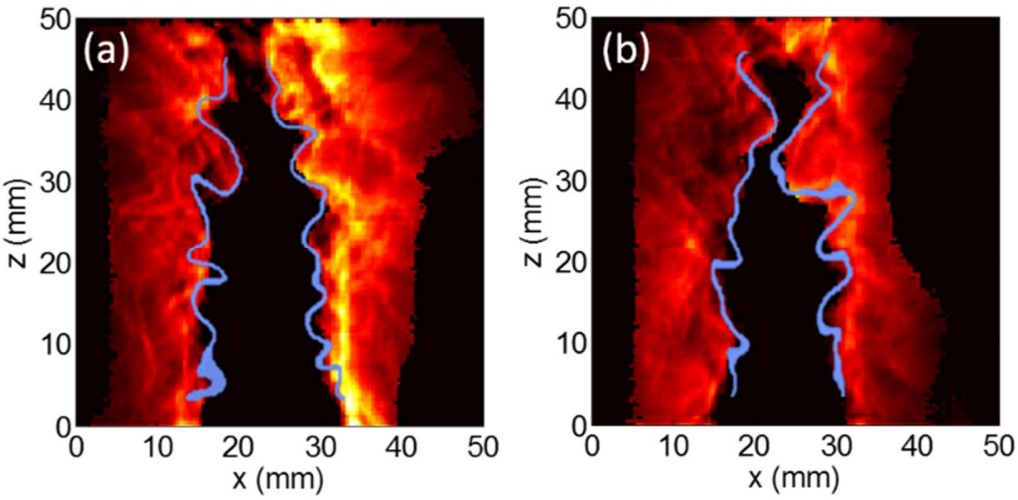

Figure 2-6. Comparison between PLIF and TC at two other instances.

2.4 Capabilities and Limitation of TC and PLIF

After the above comparison, the sections discusses the capabilities and limitations of each technique observed from such comparison.

First, the comparison shows the differences in spatial resolution between the TC and PLIF. The TC measurement contained more imaging elements than the PLIF measurement (a total of ~2 × 10^6 voxels in TC versus ~1 × 10^6 pixels in PLIF). However, due to the volumetric nature of TC, the PLIF measurement had a superior pixel resolution in a plane as illustrated Figure 2-5(d), which shows a zoomed-in view of a small region of Figure 2-5(c) so that discrete voxels and pixels can be seen. As shown, each pixel corresponds to 0.09 mm (where pixels were binned 2 ×2 after readout) on the PLIF measurements, and each voxel corresponds to 0.39 mm on the TC measurements. Therefore, while the TC technique can resolve the 3D nature of turbulent flames, it still cannot compete with PLIF in terms of in-plane resolution. Further research is ongoing in our group to improve the spatial resolution of the tomographic technique while maintaining its temporal resolution.

Second, 3D flame properties and statistics can be obtained from TC to overcome the 2D limitation of PLIF. A notable example involves the measurement of the curvature of the flame front [67, 68] (while PLIF can only provide the measurement of 2D curvature in a 2D plane). We first define 2D and 3D curvature as used here. 2D curvature used is defined following ref. [68]. For example, the 2D curvature at point on the flame front in an *x*-*z* plane is defined as:

$$K_{xz} = \frac{\dot{z}\ddot{x} - \dot{x}\ddot{z}}{\left(\dot{x}^2 + \dot{z}^2\right)^{\frac{3}{2}}} \tag{2-2}$$

where *x* and *z* represent the coordinates of the target point along the flame front, and the first-order derivatives, and the second-order derivatives (both defined along the flame front). The

definition in Eq. (2-2) was discretized using a three-point finite-differencing scheme [68] into the following format:

$$K_{xz} = \frac{8\left[x_{i-1}\left(z_{i+1} - z_i\right) + x_i\left(z_{i-1} - z_{i+1}\right) + x_{i+1}\left(z_i - z_{i-1}\right)\right]}{\left[\left(x_{i+1} - x_{i-1}\right)^2 + \left(z_{i+1} - z_{i-1}\right)^2\right]^{\frac{3}{2}}} \tag{2-3}$$

where the index i represents the i^{th} point along the flame front. The 2D curvature in other planes was defined and discretized in a similar way as shown in Eqs. (2-2) and (2-3). This chapter primarily examined the 2D curvature in the x-z plane (i.e., K_{xz}, also referred to as the vertical curvature).

For this study, the PLIF measurements shown in Figure 2-5(c) and Figure 2-6 provide the curvature in the vertical direction (i.e. K_{xz}) of the flame front on the central plane, while the 3D measurements can overcome such limitation to not only provide 2D curvature on the entire flame front but also 3D curvature. Figure 2-7(a) shows the K_{xz} of the left branch of the flame shown in Figure 2-5(c), calculated using the TC and PLIF measurements. The horizontal axes, L_{PLIF} and L_{TC}, were defined as the coordinate along the flame front based on the PLIF and TC image, respectively. As seen, while there are disagreements (e.g., between points 1 and 1', and 2 and 2') for reasons discussed previously, general agreement is observed. Processing both the PLIF and TC measurements at multiple instances leads to the statistics shown in Figure 2-7(b), illustrating the similarities and differences in 2D curvature obtained in the central plane of the flame. Due to the volumetric nature of TC, K_{xz} can be measured across the entire flame, as shown in Figure 2-7(c).

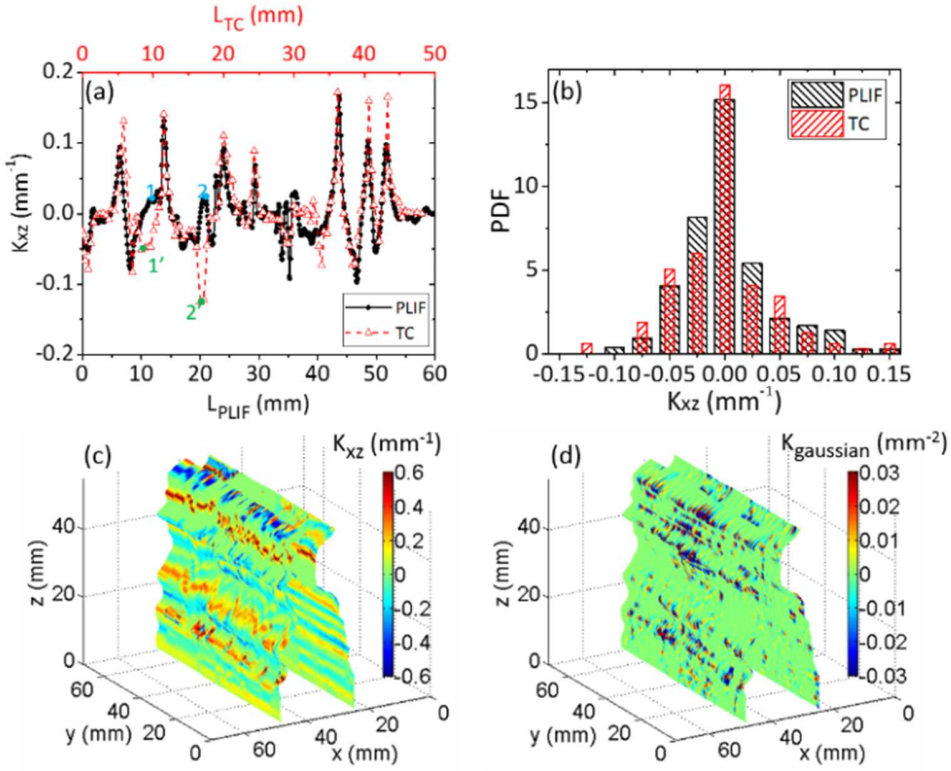

Figure 2-7. Panel (a): Comparison of K_{xz} along flame fronts obtained by PLIF and TC. Panel (b): Comparison of the PDFs of K_{xz} obtained by PLIF and TC on the central plane of the flame. Panel (c): Instantaneous 3D measurement of K_{xz} by TC. Panel (d): Instantaneous measurements of Gaussian curvature by TC.

Third, the 3D TC technique can also lead to measurement of 3D curvature on the entire flame, as shown in Figure 2-7(d). In contrast to the 2D curvature, the 3D curvature can be defined in multiple ways, and three of the definitions are examined: the principal curvatures, the mean curvature, and the Gaussian curvature. The principal curvatures at a given point on a 3D surface are defined in the following steps [69]. First, the normal vector of the 3D surface at the given point is determined. Second, normal planes, defined as planes crossing the normal vector, can be determined. Each normal plane intersects the 3D surface to form a 2D curve, and a 2D curvature at the given point can be determined along the curve following Eq. (2-2). Finally, the principal curvatures are defined as the most positive and most negative 2D curvatures (i.e. K_{max} and K_{min}) found in step two among all normal planes. Here, the algorithm described in [70] was used to determine the principal curvatures from the 3D reconstructions. Once the principal curvatures are

determined, the mean and Gaussian curvatures then are defined as the average and the product of the principal curvatures [70, 71] (i.e., $K_{mean} = 1/2(K_{max} + K_{min})$ and $K_{gaussian} = K_{max}K_{min}$), respectively. Physically, the principal curvatures quantify the two steepest curvatures (both in the positive and negative directions) at a point, and the Gaussian curvature provides information on the overall 3D structure of the surface at the point. A Gaussian curvature greater than 0 indicates an elliptic (i.e., sphere-like) surface at the given point, smaller than 0 a hyperbolic (i.e., saddle-like) surface, and equal to 0 a parabolic (i.e., cylinder-like) or planar surface [71]. In the last case, when the Gaussian curvature is equal to 0, the principal curvatures are further examined to differentiate a parabolic surface from a planar surface: it is a parabolic surface when only one of the principal curvatures is equal to 0 and it is a planar surface when both are. For example, regions with positive values of $K_{gaussian}$ seen in Figure 2-7(d) had an elliptic local surface shape, regions with negative values a hyperbolic surface pattern, and regions with zero value a parabolic surface or a planar surface (it is a parabolic surface when only one of the principal curvatures is equal to 0, and it is a planar surface when both are). Of course, such characterization enabled by 3D measurements is unobtainable from any 2D component of the curvature (e.g., K_{xz}).

2.5 Summary

In summary, the goal of this chapter was to describe the development, implementation, and a direct experimental validation of the 3D TC technique. The validation was accomplished by a comparison between a 3D diagnostic (tomographic chemiluminescence, TC) and an established 2D diagnostic (PLIF based on CH). Both diagnostics were applied to a turbulent flame simultaneously. The TC measurements were performed in a target volume of 50.5 × 50.5 × 50.5 mm^3, and the PLIF measurement was performed across the central plane of this volume. The 2D PLIF measurements were then directly compared to the 2D cross-section of the 3D TC

measurements across the central plane. Such comparison not only serves as a validation of 3D measurements but also illustrates the capabilities and limitations of both techniques. For example, the comparison shows that for the TC demonstrated in this chapter, the PLIF technique offers superior temporal and spatial resolution in a plane, while the TC technique enables more total imaging elements within a volume and provides information unobtainable from 2D measurements, such as the 3D curvature of the flame front.

Chapter 3 4D Flame Topography and Curvature Measurements at 5 kHz on a Premixed Turbulent Bunsen Flame Using TC

3.1 Introduction

Turbulent premixed combustion has found widespread applications in practical combustion systems, and a fundamental understanding of such flames is essential to the efficient operation of these systems. However, the complicated governing processes and their intricate interactions are not fully understood yet, and many open questions still exist and hinder the development of predictive combustion models [51, 72-74]. As result, significant research efforts, both numerical and experimental, have been invested to resolve the governing processes involved in turbulent premixed flames [51, 75, 76]. Due to the continued growth of computational power, DNS (direct numerical simulation) and LES (large eddy simulation) are becoming increasingly feasible to simulate the 3D (three-dimensional) and time-dependent structures of turbulent premixed flames [77-79]. Corresponding experimental data, 3D data with adequate temporal resolution (i.e. 4D), have therefore been long desired for comparison against numerical simulations and are ultimately needed to fully understand the underlying processes.

However, well-established experimental techniques have been targeted for measurements at a point, such as coherent anti-Stokes Raman scattering (CARS), along a line such as spontaneous Raman scattering, or across a plane such as planar laser-induced fluorescence (PLIF) [1]. With the recent advancements in lasers, cameras, computational technologies, and imaging processing algorithms, it has become feasible to contemplate 4D experimental measurements with the desired spatiotemporal resolutions to resolve turbulent flames. Several approaches are being actively pursued, and initial demonstration measurements have been reported. These approaches can be broadly divided into two categories, the scanning approach and tomography approach, as briefly

introduced in chapter 1. Here a thorough review of techniques in the two categories is presented. The scanning approach scans a planar technique to obtain a series of 2D measurements sequentially, and these 2D measurements can then be combined to form an effectively instantaneous volumetric measurement when the scanning is performed rapidly. Demonstrations have been performed to obtain 4D measurements by the scanning of the laser sheet for PLIF [80-82], planar Mie scattering [35], and planar laser-induced incandescence [41]. With current high-repetition-rate lasers and scanning technologies, 4D measurements with temporal resolution near 1 kHz and a spatial resolution on the order of 1 mm in the direction of scanning [80-82] are feasible. Multiple lasers can potentially be used to improve the temporal and spatial resolution at the cost of complexity and capital investment [41].

In contrast to the scanning approach, the tomography approaches obtains 4D measurements volumetrically and instantaneously without scanning. Similar to the scanning approach, the tomography approach can be used in combination with a range of signal generation mechanisms, ranging from absorption spectroscopy [83, 84], Mie scattering [22, 46], chemiluminescence [37, 38, 49], and particle imaging velocimetry (PIV) [8]. In contrast to the scanning approach, higher temporal resolution (up to 20 kHz [85]) in larger measurement volumes (on the order of 10 × 10 × 10 cm [38]) have been reported for the tomography approach because these techniques do not require the physical scanning of the illumination laser sheet. A comprehensive comparison of all the techniques in both categories, though highly valuable in the authors' opinion, is beyond the scope of the dissertation. For more in-depth discussions about the capabilities and limitations of individual techniques, the readers are referred to these following references: sheet-scanning PLIF [86], tomographic PIV [8], tomographic chemiluminescence [48], sheet-scanning Mie scattering [35], and tomographic Mie scattering [46].

Within the above context, this chapter reports 4D flame measurements at a repetition rate of 5 kHz using the TC technique validated in Chapter 2. This chapter reports measurements of 3D properties of a highly turbulent flame with temporal resolution of 0.2 ms. The measurements were performed on the same Bunsen flame as shown in chapter 2 [52]. The data reported in this chapter included 3D flame topography, position, and 3D flame curvature measured with a repetition rate of 5 kHz (an exposure time of 0.2 ms) and a nominal spatial resolution of 0.55 mm in all three spatial directions. These results were obtained in a measurement domain ~ 70 (width) × 70 (depth) × 105 (height) mm^3, sufficiently large to capture the entire flame in each tomographic measurement.

3.2 Experimental Arrangement

Figure 3-1 illustrates the experimental setup schematically from the top view and the coordinate system used in this chapter. The setup used a total of six complimentary metal-oxide semiconductor (CMOS) cameras to record tomographic chemiluminescence (TC) from a Bunsen flame. The burner was designed to produce a 2D Bunsen flame (an envelope flame [51]). The specifics of this burner (e.g., the flow passage structures and turbulence generating grids) have been detailed previously in chapter 2 and also in [52, 57, 58], and a brief summary is provided here again. The burner consisted of three parts (part I, II, and III as shown). The central part (part II), with a width (W) of 25.4 mm and a length (L) of 50.8 mm, generated the target flame. The central rectangular tube was filled about half-way with stainless-steel beads, and a turbulence-generating grid was installed just upstream of a hexagonal matrix to wrinkle the target flame. The two parts on the side (parts I and III) generated the pilot flames to stabilize the target flame. Fed with premixed methane and air at an equivalence ratio of about 1 and a bulk velocity of 5 m/s, the burner stabilizes a flame about 100 mm in height. Hot wire anemometry was performed in the cold flow

to characterize the turbulence. At a height 4 mm above the burner exit, the turbulent Reynolds number based on the integral scale was measured to be about 2,400 in the central region of the burner. The exit plane of the burner was defined as the *x*-*y* plane, with the origin defined as the center point of the exit plane, the *x* axis the central line along the width direction, and the *y* axis the central line along the length direction as shown. The *z* axis was defined along the flow direction (i.e., the height direction).

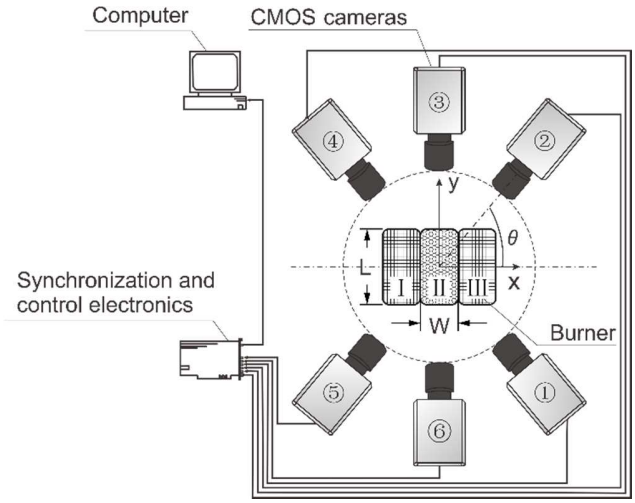

Figure 3-1. Schematic of the experimental setup.

The TC diagnostics involved cameras (2 Photron SA-4, 2 Photron SA-5, and 2 Photron SA-Z cameras) arranged as shown in Figure 3-1. All cameras were aligned in the *x*-*y* plane and their orientations were specified by θ, defined as the angle formed by the optical axis of a camera relative to the positive *x* direction as shown. The focal length and *f*-number of the lenses used on camera 1 through 6 were, respectively, 60 mm and 2.8, 35 mm and 1.4, 24 mm and 2.0; 50 mm and 1.2, 58 mm and 1.2, and 35 mm and 1.4. All these chemiluminescence cameras were used without optical filters for the consideration of signal level and temporal resolution. Thus, the chemiluminescence measurements did not discriminate CH chemiluminescence from that of other excited state species (though the signal was primarily due to CH* in the visible range, as the

cameras did not have sensitivity in the UV range and the lenses were not UV transparent). To minimize the effects of emissions contributed from other species such as CO*, this chapter extracted the inner flame edges from the 3D reconstructions to separate the chemiluminescence emissions caused by CH* from those caused by combustion products. The operation of the cameras was synchronized using control electronics, and the camera control and image acquisition were centralized on a computer as shown. All six cameras were operated at a frame rate of 5 kHz and an exposure time of 0.2 ms, equaling the reciprocal of the framing rate.

The next step in the experiments was to perform a view registration to determine the orientation and position of all the cameras [28, 30]. In the view registration process, a calibration target with known dimensions and patterns was placed at the location where the target flame was expected. Images of the calibration target were acquired by all the cameras, with a set of examples shown in Figure 3-2. This chapter used a calibration plate with square patterns as shown, and the size of each grid is 2.5 mm (best seen on Figure 3-2(d), where the camera was aligned almost perpendicular to the calibration plate). As shown in Figure 3-2, due to the different positions and orientations of each camera, each field of view showed a different degree of distortion and magnification. With the lens parameter known for each camera, a view registration program was applied to analyze such distortion and magnification and determine the location and orientation of each camera. The orientation of camera 1 through 6 was determined to be θ =305.7^{o}, 50.1^{o} , 90.4^{o}, 134.5^{o}, 227.1^{o}, and 269.7^{o}, respectively, with an accuracy estimated to be within ±0.5^{o} [30].

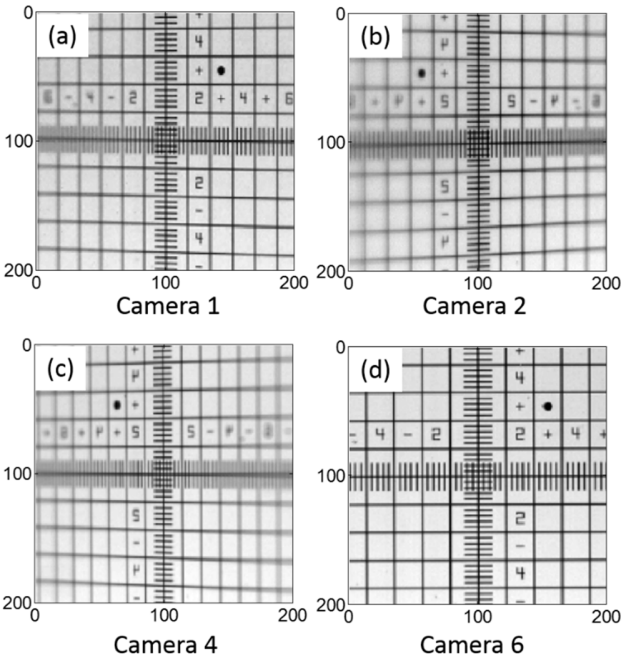

Figure 3-2. Panel (a) - (d): calibration images obtained by camera 1, 2, 4 and 6, respectively.

Figure 3-3 shows a set of example images (termed *projections*) captured simultaneously by cameras 1 through 6. As mentioned before, these projections were captured with a frame rate of 5 kHz and an exposure time of 0.2 ms. All projections had a pixel resolution of 900 × 600 pixels, and each pixel corresponded to a physical dimension of ~ 0.12 × 0.12 mm^2. Before leaving this section, it is worthwhile to comment on the factors considered in our choice of the temporal and spatial resolution of these measurements. The cameras used in this chapter can all operate at a maximum *frame size* of 1024 × 1024 pixels up to a certain frame rate (3.6 kHz for the SA-4, 7 kHz for the SA-5, and 20 kHz for the SA-Z), and their frame size began to decrease when the cameras are operated at higher frame rates. Therefore, these measurements were designed primarily by balancing the tradeoff between the frame rate and the frame size achievable by the cameras. A secondary consideration involved obtaining an optimal match between the shape of the target flame (which had a height larger than width and length) with the imaging area on the camera chip.

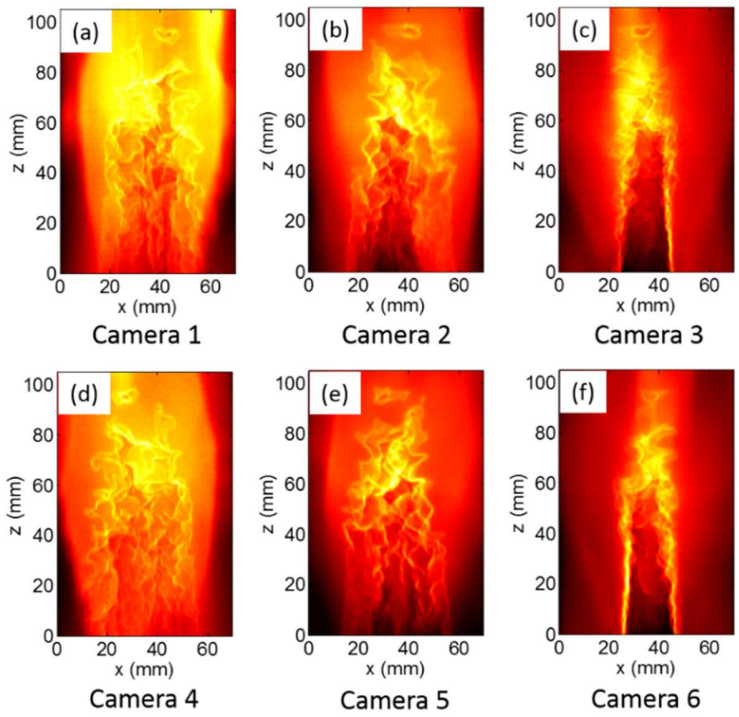

Figure 3-3. Panel (a) - (f): a set of example projections measured by camera 1 through 6, respectively.

3.3 Tomographic Reconstruction

The projections shown in Figure 3-3 were used as inputs to a tomographic reconstruction algorithm (which has been introduced in Section 2.3) to obtain the 3D distributions of the chemiluminescence. In this measurement, the measurement volume had a dimension of 70 (x direction) × 70 (y direction) × 105 (z direction) mm^3, and it was discretized into 128 × 128 × 192 voxels (i.e., I = J = 128 and K = 192), resulting in a total of 3,145,728 voxels. Under this discretization, the voxels were cubical with a dimension of 0.55 mm, representing the spatial resolution of the 3D measurements in all three directions. The choice of such a voxel dimension was due to two considerations. First, the voxel dimension was designed to be smaller than the spatial blurring during the 0.2 ms exposure time of the measurements to obtain the finest spatial resolution possible. An independent nanosecond CH PLIF measurement was performed on this

flame, which showed that the maximum movement of the flame front was approximately 1 mm over 0.2 ms. With the magnification used in the projection measurements, 1 mm corresponded to approximately 9 pixels. Therefore, the 3D measurements reported here were blurred by up to 9 pixels (or equivalently 1 mm). Hence, a voxel dimension of 0.55 mm was smaller than such blurring in most of the regions. Measurements with a shorter integration time (using 6 SA-Z cameras or 6 intensified cameras, for example) could reduce the blurring and warrant the use of finer voxels. Second, the choice of the voxel dimension also needs to take into consideration the computational resources and the number of projections, both of which are elucidated by Eq. (2-1). The length of P was ~3.2×10^6 (600 × 900 pixels/camera × 6 cameras), and the length of F ~3.1×10^6 (128 × 128 × 192 voxels). As a result, the scale of the *PSF* matrix was on the order of 3.2×10^6 rows and 3.1×10^6 columns, and the total number of elements in the *PSF* was therefore on the order of 10^{13}. Even though the *PSF* is sparse [22, 46] and various techniques have been implemented to exploit such sparsity and reduce the memory requirement for its storage [2, 49], the memory requirement here was still on the order of 100 GB (and the reconstructions in this chapter were performed on two customized workstations, one with 256 GB of RAM and the other 512 GB). Furthermore, when the length of F (i.e., the number of unknowns) exceeds that of P (the number of equations), Eq. (2-1) becomes underdetermined. Several possible approaches could help to overcome these issues and enable finer voxels, including the use of *a priori* information in the reconstructions via regularization [44, 49, 87], the use of more cameras to provide more projections, or the application of the same cameras to target a smaller measurement volume.

Using the reconstruction scheme discussed above, Figure 3-4 shows a set of sample results of the 3D reconstructions obtained. Figure 3-4(a) shows the 3D reconstruction obtained using the projections in Figure 3-3 as inputs. Figure 3-4(a) was formed based on an iso-surface of the flame

determined by a thresholding method. The thresholding method determined the iso-surface in three steps. First, the 3D reconstruction was performed using projections. Second, a background signal level was determined from the projections. Third, a threshold value was set, and the 3D reconstruction obtained in step 1 was divided into two zones based on the threshold value: a zone with chemiluminescence signal higher than the threshold value (considered to be the flame zone) and another zone with chemiluminescence signal lower than the threshold value (considered to be the *no-flame* zone). This step was especially important because some chemiluminescence was not from the flame surface.

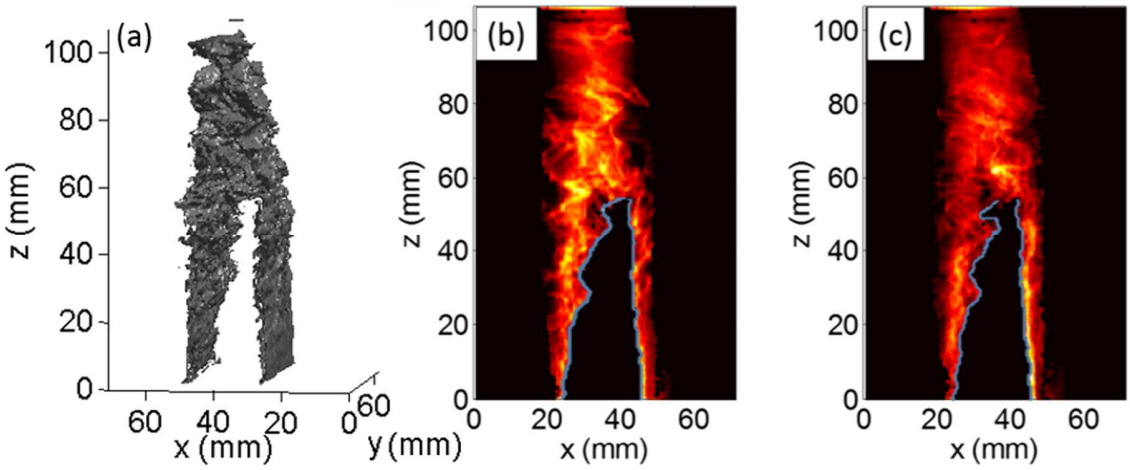

Figure 3-4. Panel (a): An example 3D tomographic reconstruction of the target flame. Panel (b): 2D cross-sectional view of the 32nd layer with extracted flame front overlapped. Panel (c): 2D cross-sectional view of the 96th layer with the extracted flame front overlapped.

To present a closer examination of the reconstructed flame topography and the performance of the above thresholding method, Figure 3-4(b) and 4(c) show the cross-sectional view of the 3D reconstruction at two different *y* locations overlapped with the flame front extracted by the thresholding method. Figure 3-4(b) shows the 32nd layer at y = 17.5 mm and Figure 3-4(c) shows the 96th layer *at* y = 52.5 mm, both overlapped with the corresponding flame fronts extracted, illustrating that closeness between the flame fronts extracted and the contour of the 3D

reconstruction. The flame fronts are used for the determination of the flame location and curvature, as elaborated in Sections 3.3 and 3.4. Analysis of the systematic error and verification of TC algorithm has been thoroughly discussed in our previous work, and readers can refer to ref. [49].

To further illustrate the accuracy and the temporal resolution of the measurements, Figure 3-5 shows five consecutive 4D measurements with comparison against the measured projections. Figure 3-5(a) shows five consecutive frames of projections measured by camera 3 (at $\theta = 90.4^{o}$). The changes in the flame features were unappreciable by visual examination across these five images. As a comparison to the measured projections shown in Figure 3-5(a), Figure 3-5(b) shows the corresponding view from the 3D reconstructions. Figure 3-5(b) shows the cross-sectional view of the 3D reconstruction at the central plane (i.e. the 64^{th} x-z layer at y = 35 mm) from the same view angle (i.e., $\theta = 90.4^{o}$) as the projections in Figure 3-5(a). As can be seen, both Figure 3-5(a) and 5(b) exhibited the expected overall flame topography. However, the projections shown in Figure 3-5(a) are line-of-sight measurements, and the results in Figure 3-5(b) are a 2D cross-section of a 3D reconstruction. As a result, the flame topography features in Figure 3-5(b) are generally sharper and more detailed than those in Figure 3-5(a). As an example, Figure 3-5(b) shows a small but clear feature with two dark rings at the top of the flame highlighted in the oval, which cannot be observed in Figure 3-5(a) due to the line-of-sight integrated nature. These features were caused by pockets of reactants and have been observed in independent measurements via CH PLIF. However, the 4D measurements performed in this chapter elucidate such features more clearly than planar measurements. To provide a validation to the 3D reconstructions, Figure 3-5(c) shows projections computed via a ray-tracing algorithm [65] based on the 3D reconstructions. These projections were computed along the same orientation as camera 3, and therefore are directly comparable to those shown in Figure 3-5(a). As seen, the comparison shows that measured

projections in Figure 3-5(a) agree with the computed projections in Figure 3-5(c) both qualitatively and quantitatively, supporting the validity of the 4D measurements. Of course, such agreement is necessary but not sufficient to verify the correctness of the tomography inversion.

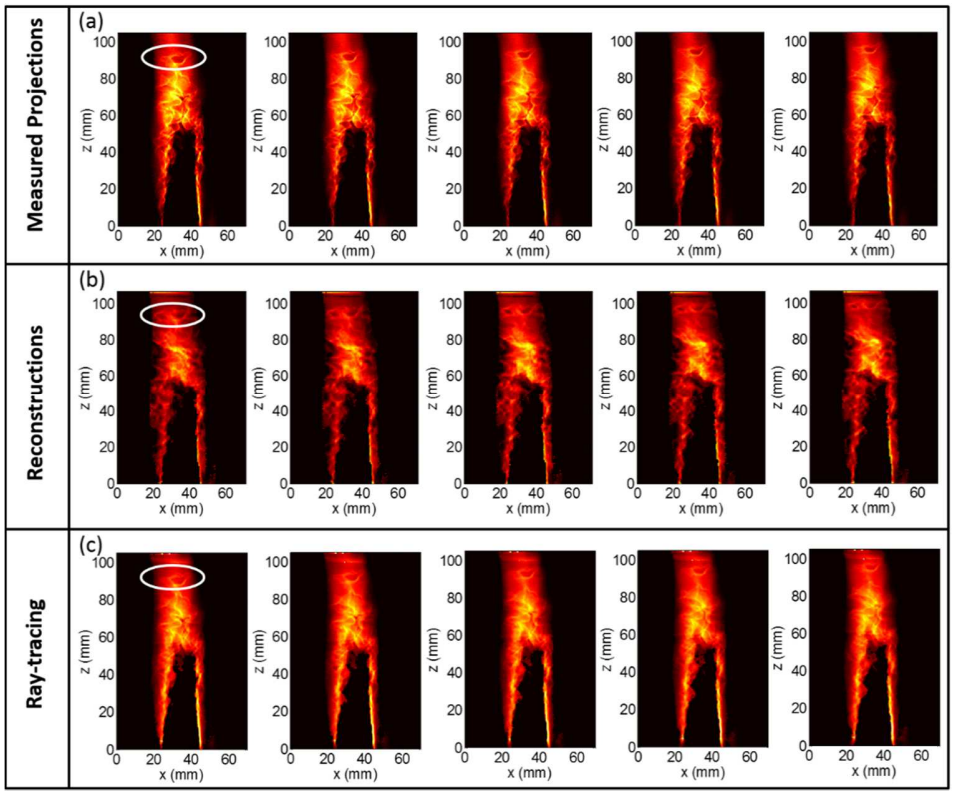

Figure 3-5. Panel (a): from left to right, five consecutive frames of measured projections from camera 3. Panel (b): from left to right, the 2D cross-sectional view at the central location of the corresponding reconstructions. Panel (c): from left to right, simulated projections at the same orientation as camera 3 via ray-tracing based on the 3D reconstructions.

3.4 Flame Location Results

After the above discussion of the 3D reconstruction, this section discusses the statistics that can be derived from such reconstructions. Processing the 3D reconstruction frame by frame, as illustrated in Section 3.3, essentially provides 4D measurements resolving the flame in all three spatial directions and also in time, enabling statistics both in the spatial and temporal domains.

This section discusses the statistics of flame locations and the corresponding PDF (probability density function [88]).

Figure 3-6 shows the statistics of the flame front at three locations derived from a series of 3D reconstructions. The three locations were shown in Figure 3-6(a) through 6(c), respectively, and they corresponded to the 32nd, 64th, and 96th layers in the reconstructions (i.e., at a location of y = 17.5, 35 and 52.5 mm). These three locations were chosen to represent the outer edge, central plane, and inner edge of the flame. The statistics shown in each panel were obtained from 40 reconstructions chosen at random times out of a total of 1000 reconstructions. Each data point in Figure 3-6 represents the location of the flame front at a particular time obtained from the 3D reconstruction. Plotting the statistics obtained from 40 reconstructions (instead of all 1000 reconstructions) improves the clarity of the figure while achieving reasonable convergence. The regions with denser data points represent regions with higher possibilities for the flame front to occur. As can be seen, the results here reveal the overall shape of the flame [52]. However, the 4D nature of the data obtained in this chapter enabled the comparison of the statistics at different locations, and the measurements at these locations were obtained simultaneously. Comparing the results shown in Figure 3-6 at three locations suggests similar overall trends but with some variations. At lower flame height (i.e., z < 20 mm), the flame fronts were relatively concentrated in two narrow branches at all three locations. The flame front became more corrugated with increasing height, and the two branches merged near 40 mm < z < 60 mm. However, differences were also observed among these three locations. For example, the overall height of the flame gradually increased from the outer edge to the inner edge. Figure 3-6(a) shows an overall flame height of ~ 60 mm at the outer edge, Figure 3-6(b) an overall height of ~ 65 mm, and Figure 3-6(c) an overall height near 80 mm. Such difference may be caused by the asymmetric flow conditions

through the burner, and the results shown here provide an illustration for the utility of multi-dimensional diagnostics in practical combustion systems.

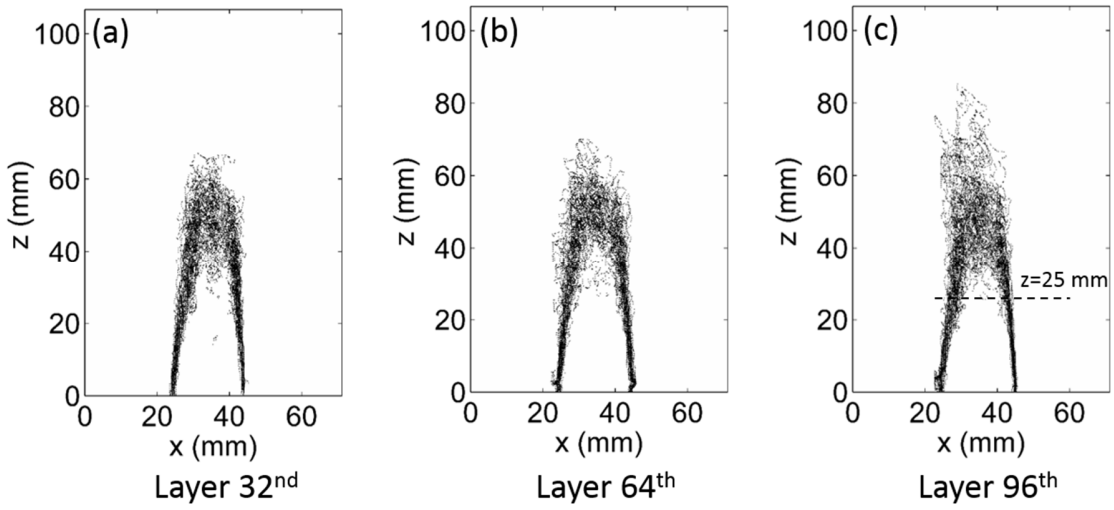

Figure 3-6. Panel (a) – (c): Statistics of flame front at layer 32nd, 64th and 96th, respectively.

Based on data shown in Figure 3-6, the PDF of the flame fronts can be obtained as shown in Figure 3-7. Again, due to the availability of information in all three spatial directions, Figure 3-7 shows the PDFs of flame fronts in three layers. Figure 3-7(a) shows the PDF of the flame front at the 32nd and 64th layers at a height of z = 25 mm, and Figure 3-7(b) that at the 64th and 96th layer at the same height. These statistics were performed using data in a range of $z \pm \Delta z$ with Δz = 0.55 mm (i.e., the thickness of one layer in the tomographic reconstruction). The intension here was to compare the PDF at the edges against that at the central plane. These results further elucidate the observations made above from Figure 3-6, that the flame fronts had similar overall trend at different locations but with some variations.

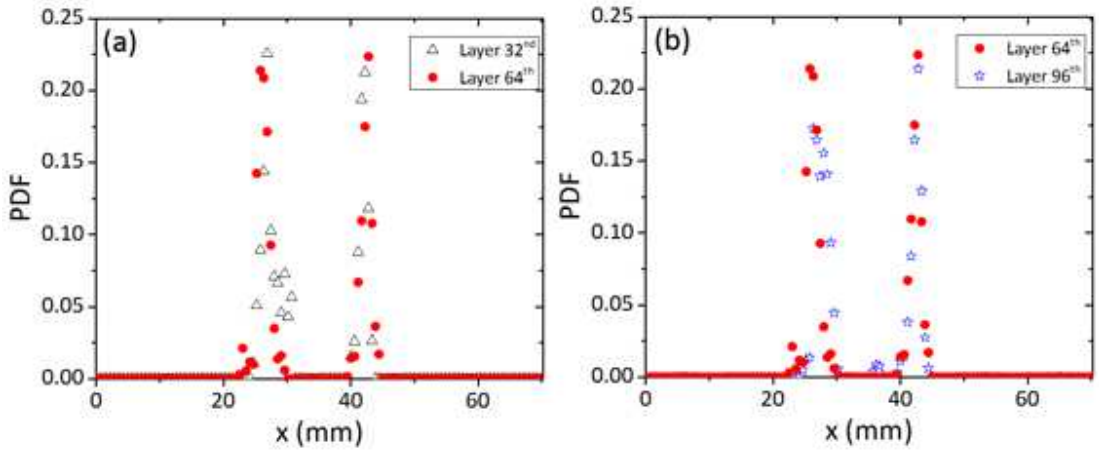

Figure 3-7. Panel (a): PDFs of flame front locations at layer 32nd and 64th and z = 25mm. Panel (b): PDFs of flame front locations at layer 64th and 96th and z = 25mm.

In summary, in this section statistics of flame location derived from the 3D reconstructions were discussed. The results illustrate that the multi-dimensional nature of the data can enable statistics in both spatial and temporal domains. Admittedly, similar statistics can be obtained using 2D or planar diagnostics. For example, statistics at various flame locations can be obtained by repeating planar measurements at multiple locations (though such measurements are not simultaneous). The next section reports the measurement of 3D flame curvature, a quantity that is difficult to obtain with planar measurements.

3.5 Curvature Results

Curvature of the flame front is an important parameter that quantifies corrugation of turbulent flame surfaces, and measurements of curvature are needed to understand the interaction of eddies [51]. However, measurement of curvature is difficult, and past efforts have been primarily limited to measurement of 2D curvature or the estimation of 3D curvature at a point of along a line. Measurement of 2D curvature is relatively straightforward with planar imaging techniques [56], for example, employing a crossed-plane configuration [71]; the 2D curvatures measured in these planes then can be used to estimate the 3D curvature along the intersection. This section reports

the measurements of full-field 3D curvature, based on the 3D reconstructions obtained in this chapter.

Based on the definition of 2D and 3D curvature introduced in Section 2.4, 2D and 3D curvatures were calculated from the 3D reconstructions. Figure 3-8(a) and 8(b) show the distribution of vertical (K_{xz}) and horizontal (K_{xy}) curvatures of the entire flame at a given moment. Here, a positive curvature value represents a convex point and a negative curvature a concave one (convex and concave were defined relative to the center *y*-*z* plane). First of all, Figure 3-8 shows the overall increasing trend of curvature, both in the vertical and horizontal directions, in the streamwise direction as expected (as the flame became more corrugated at increasing height). However, differences can also be observed between the curvatures along different directions. For instance, Figure 3-8 shows that the curvature in the vertical direction (K_{xz}) exhibited an overall magnitude larger than that in the horizontal direction (K_{xy}) (a more quantitative comparison is shown in Figure 3-11 when the PDFs of K_{xz} and K_{xy} are compared). Such difference illustrates both that the flame front is more corrugated in the streamwise direction than the spanwise direction and also the limitations of 2D flame curvature measurements. Such different patterns again reflect the limitation of 2D curvature, because 2D curvature only provides partial information of the 3D flame surface in a given plane and the information can show a different pattern in different directions.

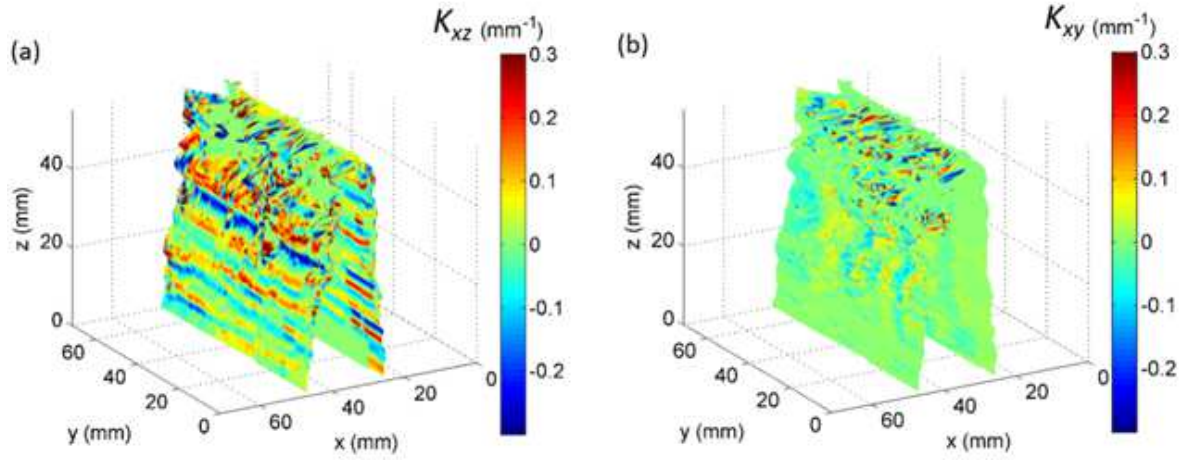

Figure 3-8. Instantaneous measurements of flame curvature in the vertical (Panel a) and horizontal (Panel b) directions.

To better illustrate the comparison between the 2D curvatures shown in Figure 3-8, Figure 3-9 shows the values of K_{xz} and K_{xy} at the central x-z plane of the flame (i.e., the 64th layer in the reconstruction). The horizontal axis (L) in Figure 3-9 was defined as the coordinate along the flame front, and L = 0 was defined at the exit of the burner. To aid the visual examination of the data, results for the left branch and right branch of the flame are plotted separately. Figure 3-9(a) shows the results along the left branch of the flame, and Figure 3-9(b) shows the right branch. Figure 3-9 elucidates the observations derived from Figure 3-8 in a more quantitative manner. These results again show that the curvatures increased in the streamwise direction as the flame became more corrugated. Also, as observed in Figure 3-8, the vertical curvature (K_{xz}) was generally larger than the horizontal curvature (K_{xy}) for both branches: for the left branch of the flame, the deviation of the magnitude of K_{xz} was calculated to be 0.0602 mm^{-1} based on the data shown in Figure 3-9(a), and that of K_{xy} was calculated to be 0.0544 mm^{-1}; for the right branch of the flame, the deviation of the magnitude of K_{xz} was calculated to be 0.0281 mm^{-1} based on the data shown in Figure 3-9(b), and that of K_{xy} was calculated to be 0.0221 mm^{-1}. Furthermore, Figure 3-9 illustrates the pattern of flame surface in terms of its alternating convex (indicated by a positive curvature) and concave

shape (indicated by a negative curvature) in correspondence to the structures created by the shear layer and the eddies generated by the turbulence grid.

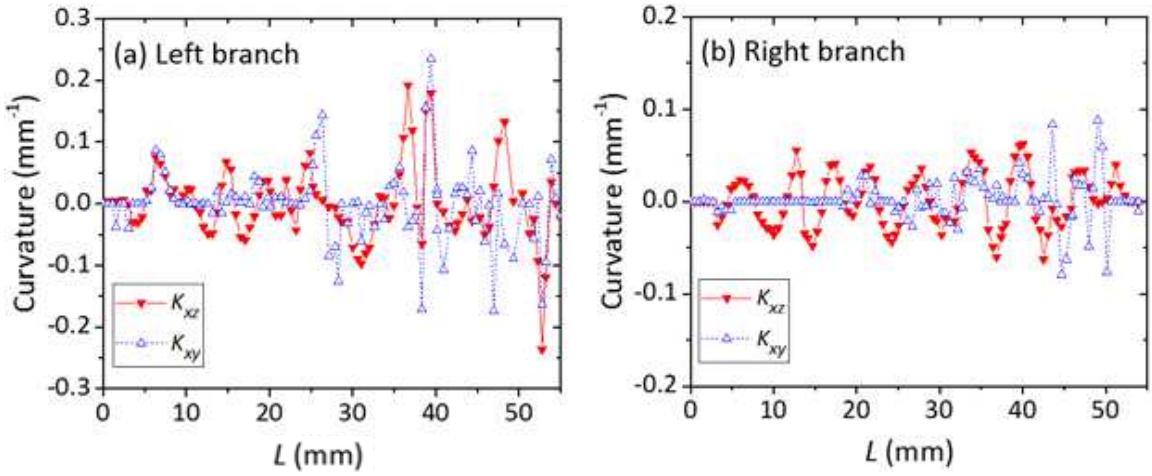

Figure 3-9. Comparisons of the vertical and horizontal curvatures at the 64th layer the left (Panel a) and right (Panel b) branch of the flame.

Below, comparison between 2D and 3D curvatures is made. First, Figure 3-10 compares the principal curvatures against the vertical and horizontal curvatures shown in Figure 3-9. Clearly, the principal curvatures encompass the vertical and horizontal curvatures as expected, because the principal curvatures are defined in the steepest directions while the vertical and horizontal curvatures are essentially curvatures along two random directions. Once the 2D and principal curvatures were obtained, their PDFs can be calculated and compared, as shown in Figure 3-11. Here, a mean curvature (K_{mean}) was defined as the average of the two principal curvatures following refs. [71, 89]. The PDFs shown here were formed by curvatures measured on one flame (i.e., one frame of 3D flame reconstruction). More specifically, the 3D flame reconstruction at one chosen moment was analyzed in the following three steps to obtain these PDFs. First, the flame front was extracted by the 3D reconstruction of the flame front at a chosen moment. As mentioned before, the flame reconstruction was performed on a total of 128 × 128 × 128 voxels (about 2 × 10^6). At this particular moment, the flame surface was identified on 25,344 voxels. Second, the

2D, principal, and mean curvatures were then calculated at all these points on the flame surface identified in the first step, resulting in a total of 25,344 measurements for each type of curvature. Third, the PDFs of the vertical, horizontal, and mean curvatures were then extracted from the results in step 2 and plotted in Figure 3-11.

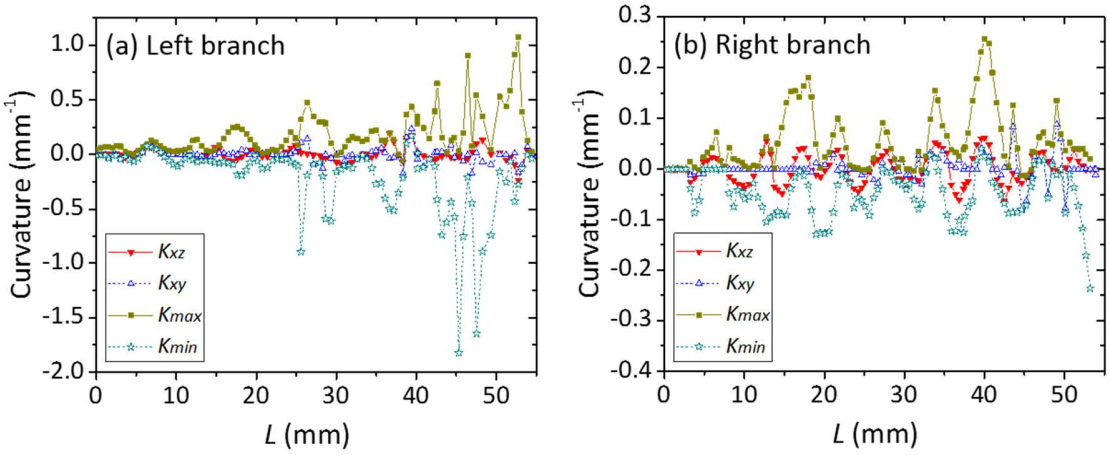

Figure 3-10. Comparisons of the vertical, horizontal, and principal curvatures of at the 64th *x*-*z* layer for the left (Panel a) and right (Panel b) branch of the flame.

Several observations can be made based on the results shown in Figure 3-11. First, the PDFs of all three curvatures are approximately symmetric with a zero mean, illustrating the stochastic nature of the turbulent flame. Second, more than 99.9% of all the data points were bounded in ±0.5 mm^{-1} for this flame, and the occurrence within ±0.3 mm^{-1} accounted for more than 99.4% of all the data points (which was also the reason that the range of the color scale in Figure 3-8 was chosen to be ±0.3 mm^{-1}). Third, the PDFs clearly show that the curvature in the vertical direction (K_{xz}) exhibited an overall magnitude larger than that in the horizontal direction (K_{xy}), an observation that agrees with the visual examination of the data shown in Figure 3-8. Lastly, due to the way K_{mean} is defined (as the average of the principal curvatures), the PDF of K_{mean} appears to be between those of K_{xz} and K_{xy}.

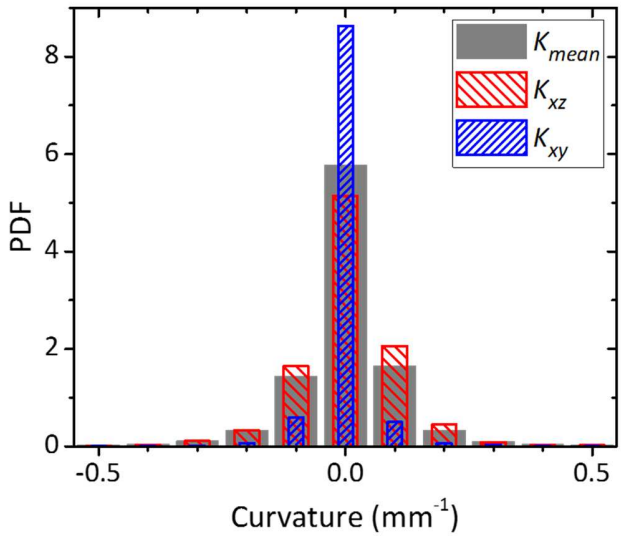

Figure 3-11. Comparison of the PDFs of 3D curvature (K_{mean}) and 2D curvatures (K_{xz} and K_{xy}).

Figure 3-12 and Figure 3-13 show the 3D curvature under the Gaussian definition. As discussed above, the Gaussian curvature indicates if the surface at a given point is elliptic, parabolic, or hyperbolic, which is an intrinsic measure of the 3D flame surface [70]. Note that other similar quantities can be defined to serve this same purpose. For instance, a shape factor, defined as the ratio of the principal curvature as discussed in ref.[71], provides the same physical meaning as the Gaussian curvature. Figure 3-12 shows the Gaussian curvature distribution on the flame front (the same flame surface shown in Figure 3-8). From Figure 3-12, it can be seen that the Gaussian curvature of most points at low flame heights (e.g., below z = 20 mm) was close to zero, which suggests that the flame shape was close to cylindrical or planar, as expected for a 2D laminar Bunsen flame. Such information cannot be obtained from 2D measurements (e.g., from the measurements of K_{xz} shown in Figure 3-8(a)), and such information is useful in practice. For example, whether a surface is cylindrical determines if how accurately a 3D curvature can be inferred from 2D imaging measurements. Figure 3-13 shows the PDF of the Gaussian curvature is between -1.0 and 1.0 mm^{-2}, a range that encompassed more than 99.9% of the data points. Similar

to the PDFs shown in Figure 3-10, the PDF of the Gaussian curvature exhibits approximate symmetry due to the highly turbulent nature of the flame. Note that the Gaussian curvature is defined as the product of two principal curvatures: the vertical axis in Figure 3-13 is shown in logarithmic scale to accommodate the range of the data. As can be seen, the PDF shows a distinct peak at zero (-0.05 mm^{-2} < $K_{gaussian}$ < 0.05 mm^{-2}) with the distribution of cylindrical and planar points marked, illustrating that a significant portion of the surface on the entire flame is cylindrical and planar. Based on the results shown in Figure 3-12, the flame surface at low *z* was the primary contributor into this portion. For a cylindrical surface, the 3D curvature (or shape of the 3D surface) can be determined from a 2D imaging measurements if the 2D imaging plane is properly oriented relative to the surface. Figure 3-12 also shows that a significant portion of the flame surface exhibited a non-zero Gaussian curvature and therefore was either elliptic or hyperbolic. For these points, the 3D shape of the flame front cannot be fully determined by 2D measurements. A number of frames were processed (e.g., as shown in Figure 3-5), and the PDFs obtained from different frames were stable.

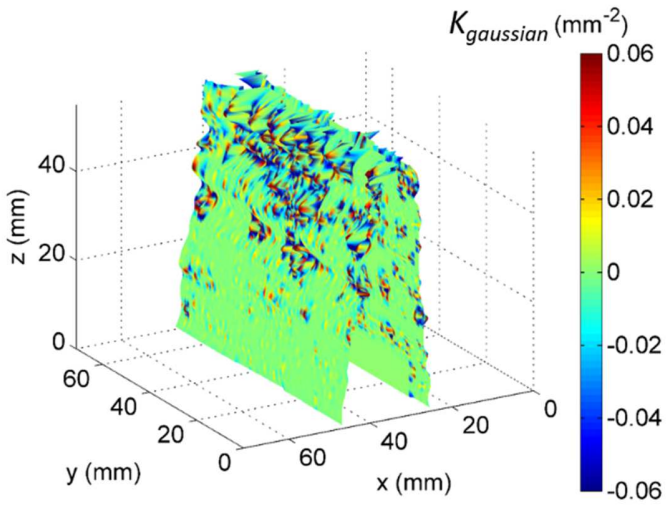

Figure 3-12. Instantaneous measurements of the Gaussian curvature.

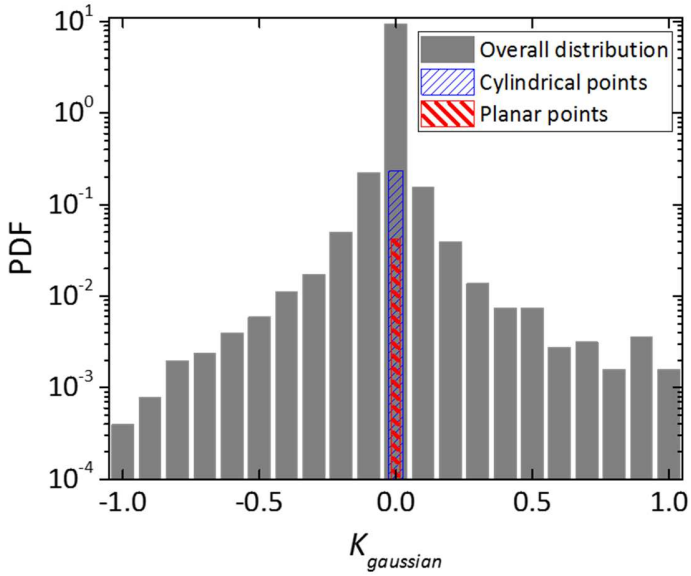

Figure 3-13. PDF of the Gaussian curvature.

Before concluding this section, we briefly discuss the uncertainty analysis and validation of the curvature measurements. As aforementioned, it is a significant challenge to measure instantaneous 3D curvature of turbulent flames, and currently there is no established technique to our knowledge. Therefore, it is difficult to perform uncertainty analysis and validation via a direct experimental approach (i.e., which may require the use of another technique that can measure 3D curvature). To obtain some preliminary results, we have performed simultaneous measurements of CH-based PLIF and TC in flames generated by this same burner under the same conditions. The goal was to obtain 3D flame topography and curvature using the TC technique described in this chapter and also a 2D PLIF image simultaneously. Then, a 2D cross-section of the flame was extracted from the 3D TC measurements across the same plane at which the PLIF was performed, so that the flame topography and curvature (2D curvature though as only 2D curvature could be calculated from the PLIF measurements). Detailed description of these comparison experiments is provided in a separated publication [34]. The results show that the curvatures extracted from the 2D PLIF image and the 3D TC measurements were in reasonable agreement, both in terms of the

instantaneous measurements and the statistics. The average difference between the magnitude of the curvatures obtained from PLIF and 3D TC was 1.3%, and 84% of the data points agree within one standard deviation (std), 95% within two std, and 98% within 3 std. Note that the difference was defined based on the magnitude of the curvature (i.e., the absolute values) such that the positive and negative errors did not cancel each other. These results should provide a reasonable estimation to the uncertainty of the curvature measurements reported here.

3.6 Summary

In summary, this chapter describes instantaneous, kHz-rate 4D measurements in a highly turbulent flame generated by a Bunsen burner. The measurements were performed using a combination of computed tomography and chemiluminescence imaging of the flame (coded named the TC technique, tomographic chemiluminescence). 6 CMOS cameras operating at 5 kHz (with an exposure time of 0.2 ms) recorded flame chemiluminescence from a volume measuring ~ 70 (width) × 70 (depth) × 105 (height) mm^3, which were used as the input for the subsequent tomographic reconstruction to obtain the 3D measurements.

Based on projection measurements of chemiluminescence emissions, 3D flame structures were reconstructed to extract 3D flame properties, and this chapter focused on the location and curvature of the flame front. For flame location analysis, the PDF of flame topography was extracted from a series of 4D measurements, and the PDFs of the flame at different spatial locations were examined. For flame curvature analysis, 2D curvature along selected orientations and 3D curvature under various definitions were calculated based on the measured 3D flame topography. The PDFs of curvature in 2D and 3D were then extracted and compared, and these results quantified the flame surface in 3D. The Gaussian curvature divided the flame surface into three categories (cylindrical, elliptic, or hyperbolic), and the PDFs provided relative portion of each category on

the entire flame surface. These results illustrate the limitations of 2D measurements and the potential of 4D diagnostics to fully resolve the spatiotemporal behavior of turbulent flames.

Finally, this chapter serves as a demonstration of the technique of tomographic chemiluminescence. Limitations of the approach lie in the number of spatial resolution elements (which is in turn limited by the total number of camera pixels) and minimum feasible exposure time. This minimum exposure time affects the spatial resolution, through the light collected by each camera pixel and through the averaging effect of the flame movement from one frame to the next. Advances in CMOS camera technology, however, will improve the sensitivity of these systems, enabling shorter exposure times and higher framing rates. With state-of-the-art CMOS cameras commercially available, measurements up to 20 kHz with similar spatial resolution reported here should be feasible. Of course, higher bulk velocities and enhanced turbulent level may require even higher framing rates and shorter exposure time.

Chapter 4 Development of Single-Shot Volumetric Laser Induced Fluorescence (VLIF)

4.1 Limitation of TC and Motivation of VLIF

The results reported in chapters 2 and 3, while illustrating the capabilities and relative simplicity of the TC technique (which relies on the nascent emissions from the flame and does not require the use of a laser), also illustrate several limitations. First, obviously, the TC technique is not applicable when there is no nascent emission such as in nonreactive flows. Second, it is difficult to separate the chemiluminescence signal from different species, and attempt to separate them typically requires the use of filtering and leads to decreased signal level. Third, the TC technique relies on the emissions from excited radicals generated by chemical reactions and thus the signal level can be relatively low and cannot be controlled. In comparison, for laser-based techniques, the signal level can be controlled by adjusting the intensity and spectral profile of the laser and can be much stronger than that generated by nascent chemiluminescence emissions. Fourth, application of chemiluminescence suffers from a tradeoff between signal level and the repetition rate of the measurements. Higher repletion rate requires short exposure time, which in turn reduces the signal level proportionally.

To overcome the above limitations of the TC technique, this chapter describes the development of a new type of 4D optical diagnostic technique by on LIF, laser induced florescence. Optical diagnostics based on laser induced fluorescence (LIF) have been extensively researched and applied in the past [15, 90]. LIF-based diagnostics have been demonstrated as a powerful and versatile tool for flow visualization and measurements. Many key flow parameters, including species concentration [91, 92], temperature [93], and mixture fraction [94-96], can be inferred from LIF measurements. However, past work has been largely limited to measurement in 1D and

2D [14, 54, 55], and it has been long desired to extend LIF to 4D measurements. Therefore, it is the goal of this chapter to develop, validate, and demonstrate the extension of LIF-based measurements to 4D. We developed a new technique, code named VLIF (volumetric LIF) for such extension. The VLIF approach combined LIF with computed tomography to obtain 3D measurements volumetrically and instantaneously.

Compared with TC, the VLIF technique is capable of overcoming the limitations of the TC technique described above. First, the VLIF technique does not need to rely on any nascent chemical species. The VLIF technique can also rely on chemical species seeded in the flow (e.g., iodine vapor used in this work). As a result, VLIF technique can be applied to any types of flow, reactive or non-reactive, at least conceptually. Second, the VLIF technique is species specific. With a carefully chosen excitation wavelength, the VLIF technique only excites a particle chemical species and the LIF signal is only generated by this chemical species. Third, the signal level of the VLIF technique can be controlled by adjusting the wavelength, intensity, and spectral content of the excitation laser. And the VLIF signal can be stronger than that from the TC technique. Fourth, the VLIF technique does not suffers from the tradeoff between signal level and the repetition rate of the measurements. As mentioned, the signal level and measurement duration of the VLIF technique are determined largely by the properties of the laser (the duration of the laser pulse, the intensity of the excitation pulse, et al) and does not depend on the exposure time any more. Therefore, measurements at higher repetition rate can be achieved without sacrificing signal level. As a result, the VLIF technique can be applied to more transient flows than the TC technique. Specifically in this chapter, the VLIF approach was demonstrated using a thick laser slab to excite the target species (iodine vapor seeded in the flow) volumetrically. The LIF signals emitted by the target species are then captured by multiple cameras from different orientations simultaneously. A

tomographic algorithm [2, 37, 38, 46-48] is then employed to reconstruct the 3D distribution of the target species based on such projection measurements.

4.2 Experimental Implementation of VLIF

The experimental implementation used to demonstrate and validate the VLIF technique was schematically illustrated from the top view as shown in Figure 4-1(a). As shown in the center of Figure 4-1(a), the target flow was a turbulent jet flow consisting of nitrogen and iodine vapor (I_2). The exit diameter of the jet was 6.35 mm. The I_2 vapor was generated by heating iodine crystals (contained in a vessel) in a water bath to a temperature of 200 ^oF (93 ^oC). A carrying dry nitrogen flow was passed through the vessel to introduce the I_2 vapor into the target flow. The mole fraction of the I_2 vapor in the target flow was therefore controlled by the vapor pressure of I_2 under the bath temperature and the flow rate of the nitrogen gas, and the maximum mole concentration of the I_2 vapor in the target flow was estimated to be 4% in the experiments performed here. The design of the seeding concentration for the VLIF measurements was similar to that for traditional PLIF measurements, involving a trade-off among several factors such as signal level, disturbance to the chemical composition of the target flow, and practicality of seeding the desired concentration. The VLIF technique was then applied to measure the relative concentration of the seeded I_2 in 3D. Note that other flow properties can be calculated as well, such as 3D mixtures fraction if the tracer can serve as a conserved scalar in the target flow (similar to the calculation of 2D mixture fraction based on PLIF). The use of I_2 tracer for mixture fraction measurement has been discussed in [96].

In some of the experiments, a rod (with a diameter of 3.18 mm) was placed at the exit of the jet, to increase the complexity of the flow structures (and also to create an easily recognizable pattern of the flow to facilitate validation). Based on the flow configuration, the following Cartesian coordinate system was defined as shown in the figure: the center point of the jet at the

exit plane was defined as the origin, the flow direction was defined as the *z* axis, and the *y* axis was defined along the direction of the rod.

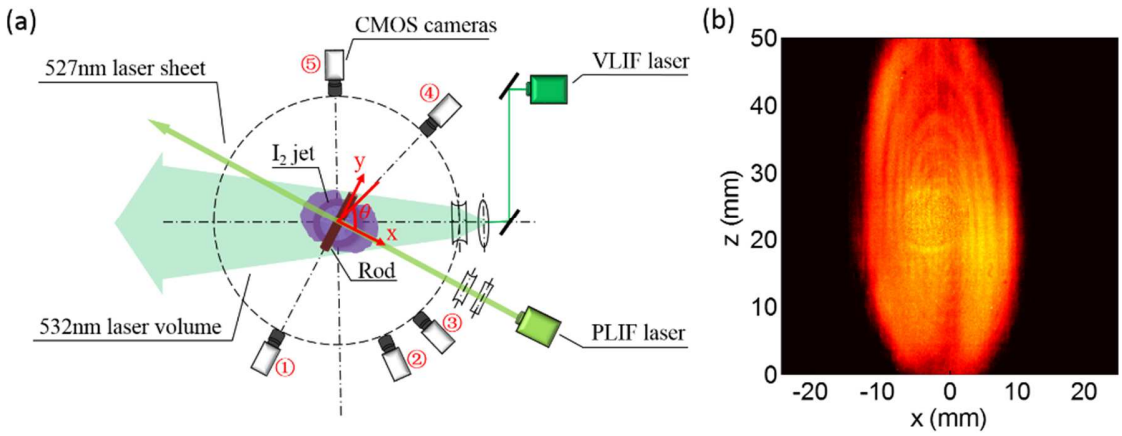

Figure 4-1. Panel (a): experimental setup from the top view. Panel (b): the spatial profile of VLIF laser intensity at $y = 0$.

The VLIF technique used the output of a pulsed Nd: YAG laser (Quanta-Ray Spectra-Physics), labeled as VLIF laser in Figure 4-1(a) at 532 nm to excite the seeded I_2 vapor. The pulse duration was about 8 ns, the repetition rate was 10 Hz, and the pulse energy was 600 mJ. The excitation laser pulses were expanded by a series of lenses into a thick laser slab so that it can illuminate a volume of 50 × 50 × 50 mm^3, and the entire target flow was excited volumetrically.

The VLIF signals generated by the volumetric excitation were then captured by five CMOS cameras (four Photron SA4s and one SA5) as shown in Figure 4-1(a). All cameras were aligned in the *x*-*y* plane and therefore their orientations were completely specified by θ, defined as the angle formed by the optical axis of a camera relative to the positive *x* direction as shown. The focal length and *f*-number of the lenses used on all cameras were 105 mm and 2.8, respectively. Each lens was equipped with a 532 ± 10 nm OD4 notch filter to block any scatter of the excitation laser. The operation of the laser and cameras was synchronized using control electronics. Prior to any measurement, a calibration target was used to determine the orientation and location of the cameras using a view registration program [30, 62]. The orientations of camera 1 through 5 were

determined to be θ = 270.0°, 311.8°, 341.9°, 73.7° and 111.1°, respectively, with an accuracy estimated to be within 0.5°. All the cameras were approximately 420 mm away from the target.

A simultaneous PLIF measurement was also performed by exciting the LIF transition of I_2 with another laser (labeled as the PLIF laser), with the purpose of providing a direct validation for the VLIF measurements. More specifically, the PLIF measurements provided a 2D image at a certain cross section of the 3D flow, which can be compared against the 3D reconstruction at the same cross section. The PLIF laser (Photonics Industries DM20 - 527 DH) generated laser pulses at a wavelength of 527 nm, with a duration of 440 ns, a pulse energy of 12 mJ, and a repetition rate of 5 kHz. The PLIF laser pulses were focused into sheets with a thickness less than 0.8 mm. The PLIF laser was aligned along the *x* axis (i.e., perpendicular to rod). To best utilize the cameras available to this project, the VLIF laser, PLIF laser, and camera 1 (which was aligned perpendicular to the PLIF laser sheet) were configured in such a way that camera 1 captured the VLIF and PLIF signal sequentially in two consecutive frames, and the temporal separation between these two frames was 0.2 ms. As a result, even though both the VLIF and PLIF techniques were able to generate single-shot measurements and therefore can be applied to highly turbulent flows, experiments in this chapter were performed under moderate turbulence levels (with a Reynolds number of 2000 defined based on the jet exit diameter), such that the flow can be approximately considered frozen during the 0.2 ms separation to make the PLIF and VLIF measurements comparable.

Before performing measurements in turbulent flows, the first step was to characterize the profile of the VLIF and PLIF laser pulses, since the LIF signal depended on both target concentration field and laser intensity distribution. To accomplish this goal, a dye cell, with a length and height both of 50 mm and a thickness of 0.5 mm, was fabricated. This cell therefore

can hold a thin layer of uniform dye solution (with a thickness of 0.5 mm). The solvent was ethanol and the dye was Rhodamine 6G, which can be excited by both the 532 nm and 527 nm laser pulses. The dye cell was then placed at different locations in the measurement volume. At each location, the dye cell was aligned perpendicular to the propagation direction of the laser pulses to be illuminated by both the PLIF and VLIF lasers. Due to the thinness of the dye solution in the cell, the integration effects in the dye were neglected and the measurement at each location was taken as the intensity distribution of the corresponding laser at that spatial location. Figure 4-1(b) shows an example of the 2D intensity profile of the VLIF laser measured at $y = 0$. The intensity profile was apparently non-uniform, necessitating such characterization *a priori*. Compiling the measurements obtained at a series of locations then provided the spatial distribution of both the VLIF and PLIF lasers.

4.3 Tomographic Reconstruction

After the characterization of the laser profiles, experiments were then performed in another dye cell (a cubical cell with a side length of 50 mm) to validate the VLIF tomographic algorithm under controlled conditions. The tomographic algorithm was based on a variation of the Algebraic Reconstruction Technique (ART), which has been validated and demonstrated extensively in the previous work for emission-based tomographic problems (such as TC) [2, 37, 47, 49, 87]. The tomography algorithm analyzes how many photons are collected on a given pixel and where these photons are emitted from the measurement volume. However, LIF-based tomography introduces a fundamental difference when the absorption is not negligible, because the intensity of the excitation laser pulse varies as it propagates through the measurement volume due to absorption, and the variation depends on the concentration of the sought distribution of the target species.

In this chapter, the VLIF problem was solved by iterating an ART algorithm on the target concentration field layer by layer iteratively. More specifically, the algorithm consisted of four steps. In the first step, the computation domain was divided into multiple layers (and the first layer was defined as the layer the VLIF laser first interacted with). In the second step, the 3D reconstruction of the concentration of the target species was performed in the first layer. The laser intensity in the first layer was only attenuated by the target species in the first layer and this attenuation can be neglected if the layer was sufficiently thin. Therefore the laser intensity in the first layer was known (i.e., identical to the incident one that characterized *a priori* as shown in Figure 4-2(a)). Therefore, with the laser intensity known, the 3D reconstruction in the first layer can then be solved by the ART algorithm. In the third step, with the 3D concentration of the target species obtained from the second step, the intensity profile of the laser exiting the first laser (i.e., entering the second layer) can then be calculated, which was taken as the laser profile in the second layer (again assuming sufficiently thin layers). Hence, the 3D reconstruction in the second layer can be performed. In the fourth step, the operations described in steps two and three were iterated on the remaining layers until convergence was achieved. Detailed description of the algorithm and its numerical validation will be elaborated elsewhere. Here we focus on the experimental validation of the algorithm and its application.

Figure 4-2 shows a set of example validation results obtained in the $50 \times 50 \times 50$ mm^3 cubical dye cell using the algorithm described above. This cell was filled with the same Rhodamine 6G solution and placed in the measurement volume. The dye solution was excited with the 532 nm VLIF laser volumetrically. The LIF emissions were measured by all five cameras, based on which a tomographic reconstruction was performed using the algorithm described above to obtain the 3D distribution of the dye concentration (which should be simply a uniform distribution because the

dye solution was well mixed). The computational domain was taken to be 50 × 50 × 50 mm^3, identical to the cubical dye cell. The domain was then discretized into 120 × 120 × 120 voxels, resulting in a 3D spatial resolution of 0.42 × 0.42 × 0.42 mm^3 in the reconstruction. The discretization was designed by a consideration of both practical and fundamental factors. Practically, the computational cost and memory requirement scale proportionally to the discretization. Fundamentally, when the number of unknowns (i.e. number of voxels) in the tomography problem exceeds the number of independent equations provided by the measured projections (i.e. number of pixels in the measured projections), the problem becomes under-determined. With the cameras and imaging optics available in this chapter, the number of pixels providing useful information was approximately 1.8×10^6, and a discretization of 120 × 120 × 120 resulted in a total of ~1.7×10^6 voxels.

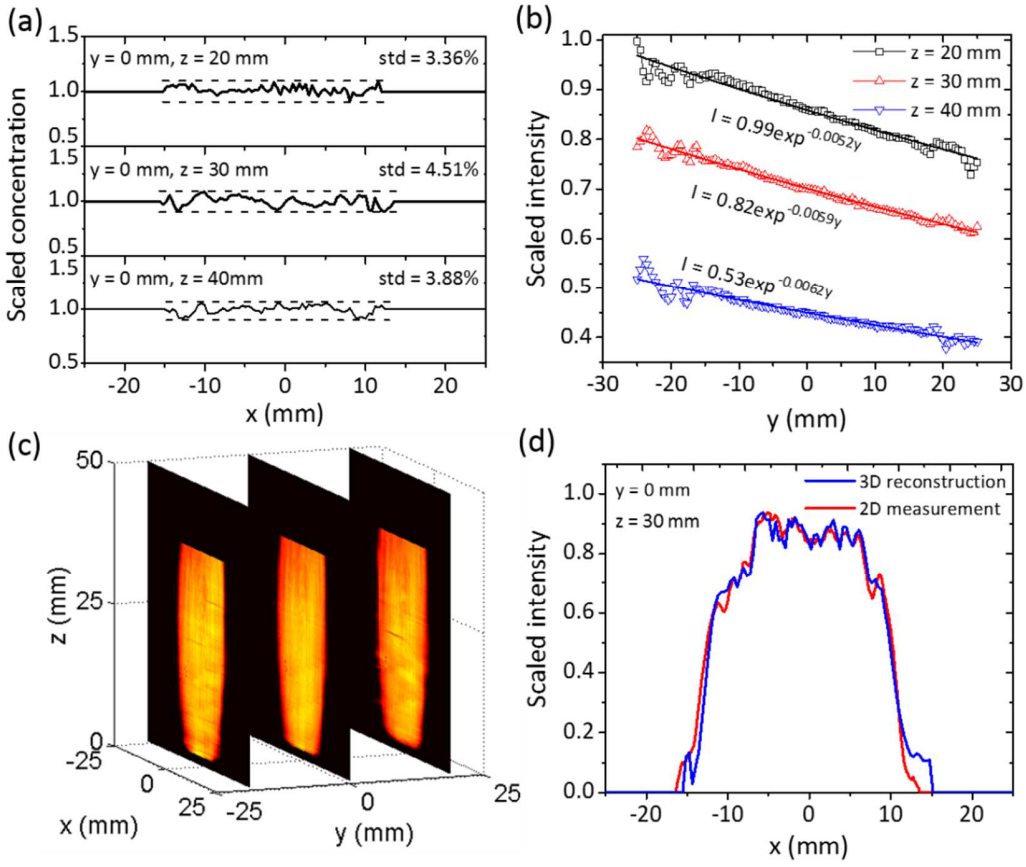

Figure 4-2. Controlled VLIF experiments performed in a dye cell. Panel (a): dye concentration at three locations obtained from 3D VLIF measurements. Panel (b): scaled laser intensity along the VLIF laser path at three different z locations (z = 20, 30 and 40 mm). Panel (c): laser intensity at three locations obtained using the 3D VLIF reconstruction algorithm. Panel (d): comparison of the laser intensity obtained by 3D reconstruction and direct 2D measurement.

Figure 4-2(a) shows the reconstructed concentration (normalized) at several z locations (z = 20, 30 and 40 mm) along the central plane of the dye cell (i.e., y = 0 mm). As seen from Figure 4-2(a), the reconstructed concentration agreed with the expected uniform distribution closely, with a std (standard deviation) less than ~5%. Reasons for such deviation and future improvement will be examined more closely at the end of this section. To confirm that appreciable attenuation occurred in these measurements, Figure 4-2(b) shows the laser intensity measured along the laser propagating direction (i.e., along the y axis) at three different z locations (i.e. z = 20, 30 and 40 mm). These measurements were made by focusing the VLIF laser into a thin sheet, propagating the sheet through the dye cell, and measuring the LIF emissions at different y locations. As seen from Figure 4-2(b), the intensity (I) of the excitation laser was attenuated appreciably due to absorption, and a fit of the data confirmed that the absorption follows the exponential Beer-Lambert relationship. The reconstruction algorithm was insensitive to the magnitude of absorption under the conditions in this chapter, primarily for two reasons. First, the absorption was not very strong (~20% in the dye cell test shown here and less than 5% in the flow measurements) and the media remained optically thin. Second, the algorithm was designed to perform reconstruction under appreciable absorption. Though it is an interesting topic for future research to examine the accuracy and applicability of the algorithm under strong absorption (i.e., in an optically thick media).

Results in Figure 4-2(c) - 2(d) provide another validation of the VLIF reconstruction algorithm in an absorbing media by exploiting the duality of the tomography algorithm. More specifically, the problem of reconstructing the concentration field with known laser intensity field (as solved in

Figure 4-2(a)) is equivalent to reconstructing the laser intensity field with known concentration field, and both problems were solved by the algorithm described in Section 4.3. Based on such duality, the VLIF algorithm was applied to reconstruct the 3D laser intensity field based on the projections measured from the dye cell under the same discretization scheme used in Figure 4-2(a). Again, in this reconstruction, the dye solution was taken as an input known *a priori* (i.e., a uniform distribution). Figure 4-2(c) shows the laser intensity at three different locations (the 20^{th}, 60^{th} and 100^{th} layer in the y direction) obtained from this reconstruction. To examine the reconstruction quantitatively, Figure 4-2(d) compares reconstructed laser intensity against that directly measured (i.e., the one shown in Figure 4-1(b)) along a line (y = 0 and z = 30 mm). As seen in Figure 4-2(d), the 3D reconstruction and the measurement agree well both at an overall and detailed level. The variation was also within ~5%, similar to that observed in Figure 4-2(a). The experiments performed here and the reconstruction algorithm also provide an approach to characterize the 3D distribution of the laser intensity.

In summary, controlled measurements were performed in a dye cell to provide experimental validation to the VLIF reconstruction algorithm. Exploiting the duality of the problem, the algorithm was validated both via comparison between reconstructed dye concentration field against the known concentration field, and also via comparison between reconstructed laser intensity field against the measured intensity field. Both validations showed an agreement within ~5%. Two major factors causing such disagreement included the reconstruction algorithm and measurement error caused by pulse-to-pulse variation of the laser intensity. First, according to our numerical simulations using phantoms, the reconstruction algorithm was able to solve the VLIF problem within 1~2% accuracy with error-free projections (here accuracy was defined following [38] as the overall difference between the reconstructed distribution and the phantom relative to

the overall magnitude of the phantom). The current algorithm was based on the iteration of the ART, and alternative algorithms (e.g., based on simulated annealing [32, 87]) are being explored to improve the reconstruction accuracy. Second, the shot-to-shot variation of the laser pulses was measured to be ~1.1% both in terms of the pulse energy and spatial distribution (defined as the std over 50 shots), while the laser profile characterization was not performed *in situ* (e.g., the 3D and 2D measurements compared in Figure 4-2(d) were taken at different times). Possible approaches to reduce uncertainty caused by this factor include the use of a more stable laser, monitoring the laser intensity *in situ* with additional cameras, or performing the measurement in the saturated regime.

4.4 Results from Turbulent Flows

With the experimental setup and tomographic algorithms developed in the previous sections, this section reports single-shot VLIF measurements of 3D distribution of I_2 vapor in turbulent jet flows.

Figure 4-3 shows a set of example projections captured by camera 1 through 5, displaying an incompletely developed jet flow with two branches generated by the rod placed at the exit of the jet. Figure 4-3(a) shows the PLIF image obtained by camera 1, and Figure 4-3(b) - 3(f) show the simultaneously measured VLIF projections by camera 1 through 5, respectively. As mentioned earlier, the VLIF projections were measured 0.2 ms after the PLIF image, and this delay was negligible for this flow (with a Reynolds number of 2000 defined based on the jet exit diameter) so that the PLIF and VLIF measurements were considered to be simultaneous. All projections had a resolution of 600 × 600 pixels, and each pixel corresponded to a physical dimension of 0.06 × 0.06 mm. Both the PLIF image and VLIF projections were single-shot measurements. Note that

the PLIF image in Figure 4-3(a) appeared clearer and sharper than the VLIF projection because the VLIF projections (Figure 4-3(b) - 3(f)) were line-of-sight integrated.

Compared with the chemiluminescence projections obtained in Figure 2-2 from chapter 2 and chapter 3, the VLIF projections shown in Figure 4-3(b) - 3(f) are of higher signal level, obtained during a much shorter duration (about 8 nanoseconds in here compared to 0.2 ms for the TC technique), and can be extended to higher repetition rate as to be discussed in chapter 5.

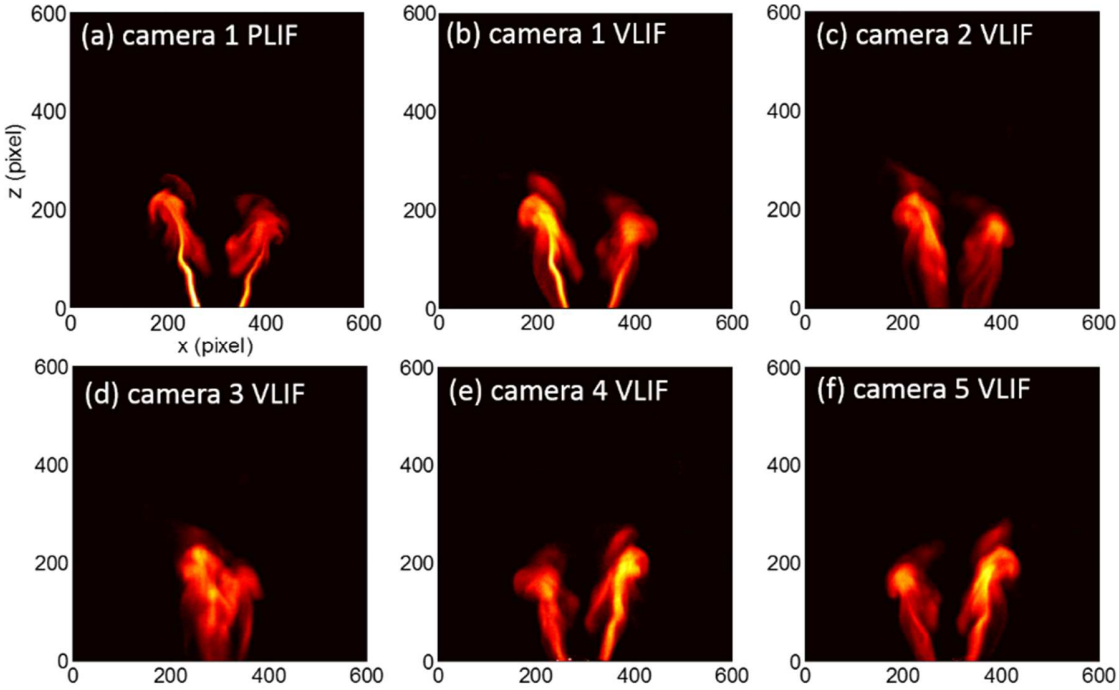

Figure 4-3. A set of example projections measured by camera 1 through 5. Panel (a): the PLIF image captured by camera 1. Panels (b) - (f): the VLIF projections captured by camera 1 through 5.

Based on the projections, the 3D distribution of the I_2 vapor concentration in the jet flow was reconstructed using the tomographic algorithm described above. Figure 4-4 shows an example reconstruction obtained using the projections shown in Figure 4-3. This reconstruction was performed in a computational domain of 35.5 × 35.5 × 35.5 mm^3, sufficient to encompass the entire target flow as seen in Figure 4-3. This computational domain was discretized into 120 × 120 × 120 voxels (~1.7 × 10^6), resulting in a nominal spatial resolution of 0.30 mm. Figure 4-4(a)

shows a 3D rendering of the relative I_2 concentration, illustrating the overall V-shape of the flow. The iso-surface value in Figure 4-3(a) was set to a numerical value of 11% of the maximum intensity of the reconstructed I_2 concentration in the domain of interest, a value chosen to provide differentiation against background noise and to preserve the contour of the I_2 concentration field. To better present the 3D reconstruction, Figure 4-4(b) shows three planar slices of the reconstruction at three different *y* locations (corresponding to the 50^{th}, 60^{th}, 70^{th} layer in the *y* direction). Figure 4-4(b) shows that the 3D reconstruction also captured the flow feature at a more detailed level. For example, the 60^{th} layer corresponded to the central plane of the jet flow (i.e. $y = 0$), and therefore the overall I_2 concentration on this layer should be higher than the other two layers due to less entrainment (more ambient air was entrained into the jet in its outer portions than the central portions, resulting in more dilution and relatively lower I_2 vapor concentration in the outer portions). This feature was clearly captured by the 3D reconstruction shown in Figure 4-4(b).

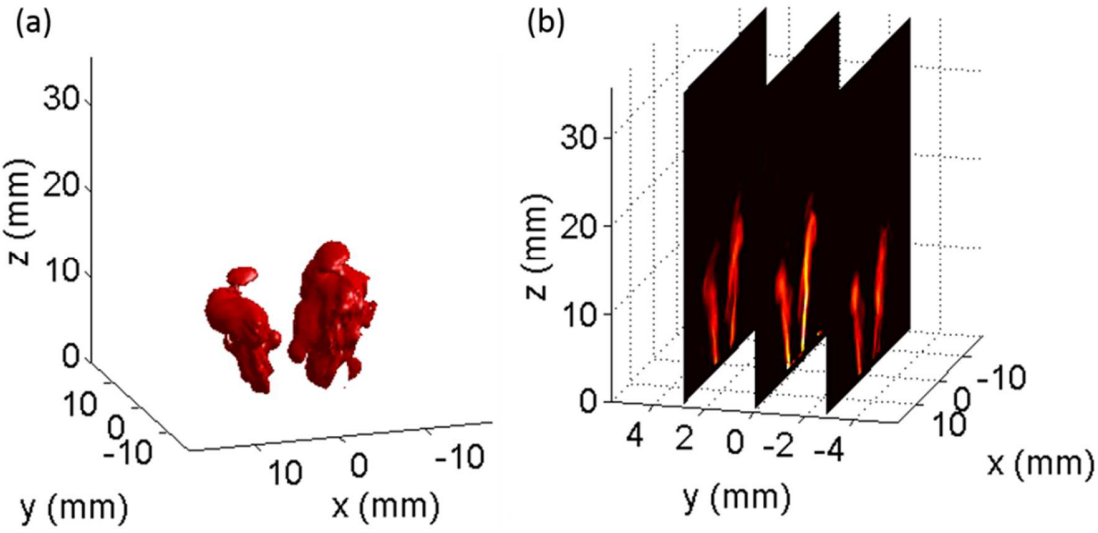

Figure 4-4. Panel (a) 3D VLIF measurement of a jet flow, Panel (b) three 2D slices of the measurement.

To further validate the above 3D VLIF reconstructions, Figure 4-5 directly compares the VLIF against the PLIF measurements. Figure 4-5(a) shows the VLIF reconstruction at the central layer

at y = 0, (i.e. layer 60th as shown in in Figure 4-4(b)). Figure 4-5(b) shows the PLIF image measured by camera 1 also at the central layer (i.e., the same image shown in Figure 4-3(a)). A comparison between Figure 4-5(a) and 5(b) suggests agreement at both overall and detailed level. For example, both the VLIF and PLIF measurements revealed the left branch to be taller and have an overall higher I_2 concentration than the right branch. The comparison between Figure 4-5(a) and (b) also shows the differences in spatial resolution between the VLIF and PLIF measurements. The VLIF measurement contained more imaging elements than the PLIF measurements (a total of ~1.7×10^6 voxels in the VLIF versus 0.36×10^6 pixels in the PLIF). However, due to the volumetric nature of the VLIF measurement, the PLIF measurement had a superior pixel resolution in a plane as shown in Figure 4-5(a) and 5(b). As aforementioned, the nominal spatial resolution of the VLIF measurement was 0.42 mm, calculated by dividing the dimension of the measurement volume with the discretization (i.e., 50 mm/120 = 0.42 mm). This nominal resolution represents the highest possible resolution that can be obtained. The actual resolution will be worse than the nominal resolution due to the factors such as measurement and reconstruction uncertainty. The comparison between VLIF and PLIF shown in Figure 4-5(c) provides a way to estimate the actual resolution. The spatial resolution of the PLIF measurements was estimated to be 0.059 mm in this chapter, sufficiently higher than of the nominal VLIF resolution. We examined which level of details captured by the PLIF can be resolved by the VLIF using the comparisons such as shown in Figure 4-5(c). Based on this examination, the actual spatial resolution of the VLIF was estimated to be 0.71 mm, which was worse than (but on the same order as) the nominal resolution of 0.42 mm.

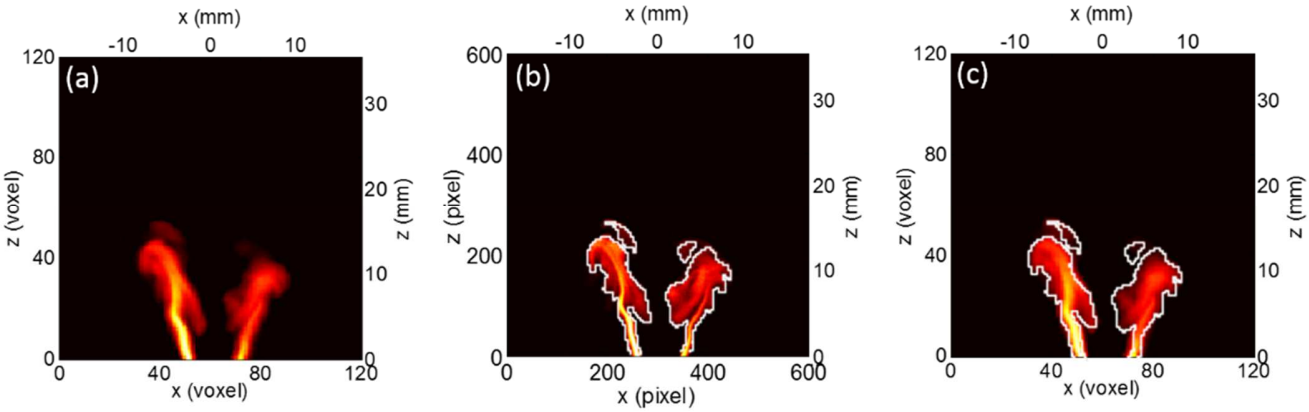

Figure 4-5. Comparison of VLIF against PLIF in an under-developed turbulent jet flow. Panel (a): the VLIF reconstruction at the central layer at y = 0. Panel (b): PLIF measurement of the flow at its central plane (captured by camera 1). White line shows the edge extracted from the image. Panel (c): panel (a) overlapped with the edge extracted from the PLIF image (i.e., the white line shown in panel (b)).

Therefore, with the current status of the VLIF technique demonstrated in this chapter, it can overcome the planar nature of PLIF and resolve the three dimensionality of turbulent flows, but still cannot compete with PLIF in terms of pixel resolution in a plane. Further research is undergoing in our group to improve the spatial resolution of the VLIF technique while maintaining its single-shot and instantaneous nature. To facilitate a more quantitative comparison, also shown in panel Figure 4-5(b) is the edge of the flow structure extracted from the PLIF image (the white lines) with a thresholding algorithm [85]. Figure 4-5(c) then overlaps the edge on top of the VLIF slice shown in Figure 4-5(a). Good agreement can be observed in Figure 4-5(a). For instance, the two detached flow regions in each branch were measured by both the VLIF and PLIF techniques.

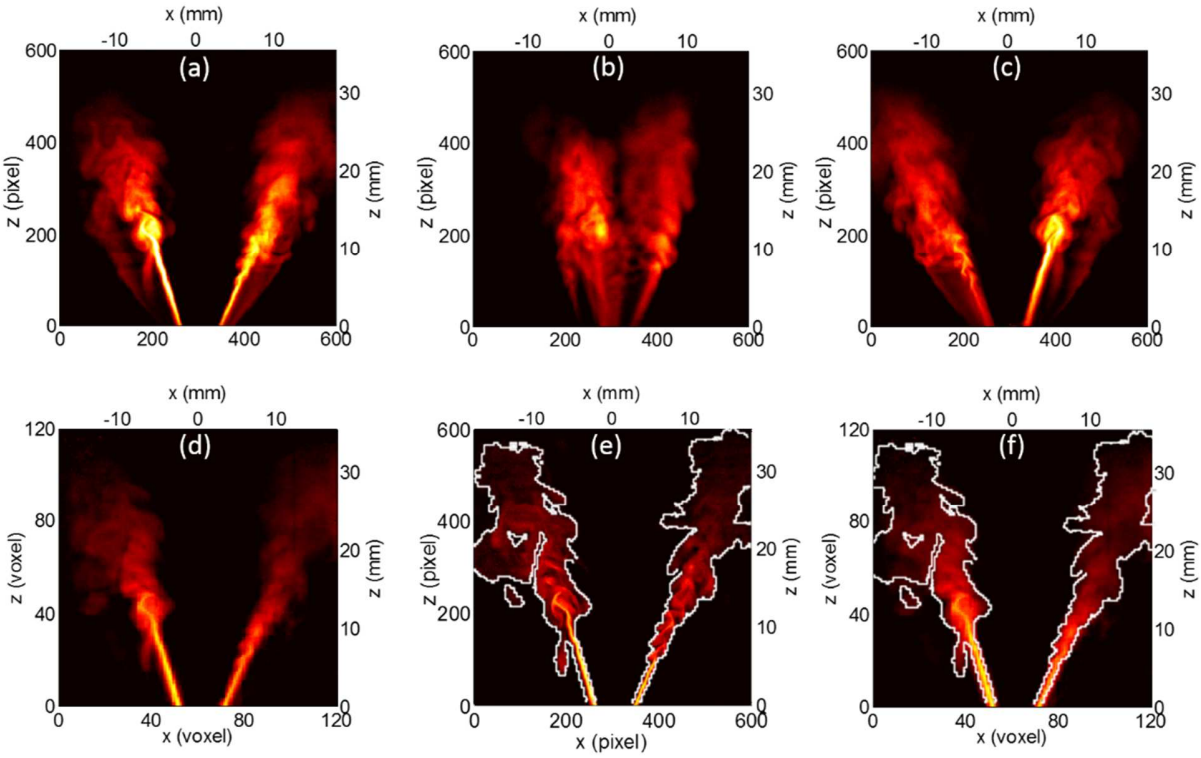

Figure 4-6. Comparison of 2D reconstructed slice against the experimental PLIF and VLIF projection in a fully developed turbulent flow. Panel (a)-(c): three of the five projections used in the VLIF reconstruction, captured by camera 1, 3, and 4, respectively. Panel (d): the VLIF reconstruction at the central layer at $y = 0$. Panel (e): PLIF measurement of the flow at its central plane (captured by camera 1). White line shows the edge extracted from the image. Panel (f): panel (d) overlapped with the edge extracted from the PLIF image (i.e., the white line shown in panel (e)).

Lastly, Figure 4-6 shows another example of the comparison between the VLIF and PLIF techniques in a fully developed turbulent flow. Figure 4-6(a) - 6(c) show three of the five projections used in the VLIF reconstruction, captured by camera 1, 3, and 4, respectively. Figure 4-6(d) - 6(f) are parallel to Figure 4-5(a) - 5(c), showing the central slice taken from the 3D VLIF measurement, the corresponding PLIF measurement and its edge extracted, and the overlap of the edge with the VLIF slice, respectively.

4.5 Summary

This chapter reports the development and validation of volumetric laser induced fluorescence (VLIF). The technique was developed to obtain single-shot measurements in turbulent flows volumetrically and to overcome some of the limitations associated with the TC technique. Single-shot VLIF measurements (with a measurement duration of a few ns) were demonstrated in a 50 × 50 × 50 mm^3 volume with a total of 120 × 120 × 120 voxels (resulting in a nominal spatial resolution of 0.42 mm in all three dimensions). The measurements were performed based on the LIF signal of iodine (I_2) vapor seeded in the flow. The VLIF technique excited the seeded I_2 vapor volumetrically by a thick laser slab. The volumetric LIF signals emitted were then simultaneously collected by a total of five cameras from five different orientations, based on which a 3D tomographic reconstruction was performed to obtain 3D measurements. To validate the reconstruction algorithm and VLIF measurements, static cell measurements and simultaneous PLIF measurements were also performed. The static cell experiments provided controlled tests to the reconstruction algorithm by the use of a dye cell with a known (i.e., uniform) concentration field. The PLIF measurement performed simultaneously with the VLIF provided a direct comparison for validation. Such comparison, besides providing a validation of the VLIF measurements, suggests that the actual spatial resolution of the VLIF technique to be ~0.71 mm, compared to the nominal resolution of 0.42 mm. The comparison also shows that at the status of the VLIF demonstrated in this chapter, the PLIF technique still offers superior spatial resolution in a plane even though the VLIF technique enables more total imaging elements volumetrically and resolves the three dimensionalities of turbulent flows.

Chapter 5 Kilohertz VLIF Measurements in Turbulent Flows

5.1 Introduction

After the proof-of-concept demonstration of the VLIF technique in the previous chapter at a repetition rate of 10 Hz, this chapter describes demonstration of VLIF measurements in turbulent flow with repetition rate up to 10 kHz. Single-shot measurements at low repetition rates (e.g., 10 Hz), besides serving as proof-of-concept and facilitating the experimental validation, are also useful for studying the spatial structures of the target flow. However, measurements at higher repetition rates are highly desired to resolve the temporal dynamics of turbulent flows and flames. Therefore, this chapter describes VLIF measurements at higher repetition rates.

As mentioned earlier, the primary limitation of the repetition rate for VLIF is the laser source, no longer limited by the tradeoff between signal level and the exposure time. Thanks to the continued advancement in laser technologies, high-power and high-repetition rate lasers have become commercially available to enable VLIF measurements at high repetition rate, and the trend of this advancement will surely continue to further push the capabilities of VLIF measurements. As an example, the chapter reports the application of a high-repetition rate laser (Photonics Industries DM30 – 527) in VLIF measurements. The laser is capable of generating laser pulses with duration on the order of a few hundred nanoseconds and with repetition rate up to 10 kHz, thusly enabling 4D VLIF measurement to 10 kHz.

Based on this new instrumentation, in this chapter, we demonstrate 4D VLIF measurements based on I_2 vapor at a various repetition rate (ranging from 1 kHz to 10 kHz) in turbulent jet flows. These measurements illustrate the capability of VLIF to provide instantaneous 4D measurements to resolve both the 3D spatial structures and also the temporal dynamics of turbulent flows. These results also provide data to allow the study of the capabilities and limitations of 4D VLIF. This

work investigated the VLIF signal level and its impact to the reconstruction accuracy under different conditions in terms of repetition rate, excitation pulse energy, and duration. Both experimental and numerical work was conducted to map out the relationship between these parameters, providing guidance to the applications of the VLIF technique under various practical requirements.

5.2 Experimental Arrangement

Figure 5-1 illustrates the experimental setup schematically from the top view and the coordinate system used in this chapter. As shown in the central part of Figure 5-1, the target flow, a turbulent jet flow consisting of nitrogen and seeded I_2 vapor, was generated from a 6.35 mm-diameter jet. The I_2 vapor was seeded into the target flow by heating a vessel containing iodine crystals. The vessel was heated by a water bath, which was held at a constant temperature of 93 °C. The nitrogen flow was passed through the iodine crystals at a flow rate of 4.5 SLPM, carrying the I_2 vapor into the target flow. The mole fraction of the I_2 vapor in the target flow was controlled by the temperature of the water bath (which controls the vapor pressure of I_2) and the flow rate of the nitrogen gas. Under the experimental conditions in this chapter, the maximum mole concentration of I_2 vapor in the target flow was estimated to be 4%.

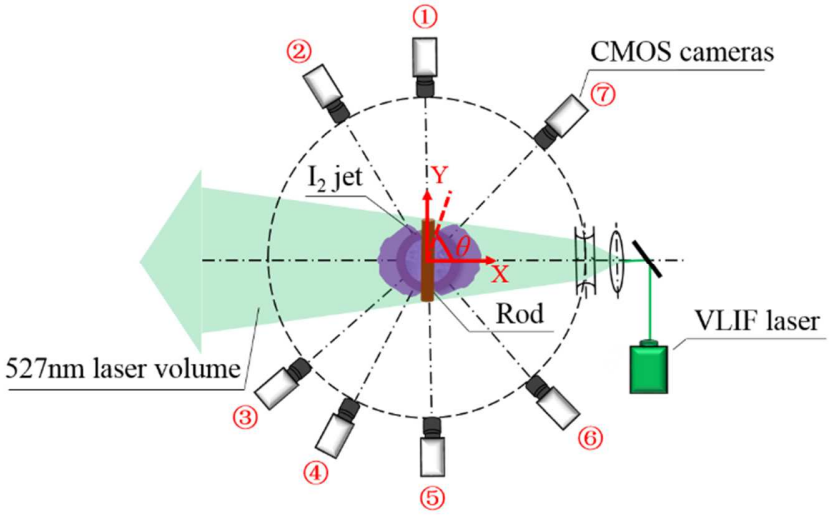

Figure 5-1. Schematic of the experimental setup from the top view

The output of the high repetition rate ND: YLG laser (Photonics Industries DM30 – 527, labeled as VLIF laser in Figure 5-1) at a wavelength of 527 nm was used to excite the seeded I_2 vapor in the flow. The VLIF laser generated pulses with varying pulse energy and duration at different repetition rate. In this chapter, the laser was operated with repetition rate from 1 to 10 kHz, with pulse energy varying between 72 mJ to 15 mJ and pulse duration between 150 ns to 450 ns. The excitation laser pulses were then expanded by a series of lenses into a thick laser slab so that the entire measurement volume of interests ($50 \times 50 \times 50$ mm^3) was illuminated. Based on the flow and optical configuration, a right-handed Cartesian coordinate system was defined as shown in Figure 5-1. The exit plane of the jet was defined as the *x*-*y* plane, with the origin defined as the center point of the jet. The *y* axis was defined to be perpendicular to the propagation direction of the laser, and the *z* axis was defined as the flow direction (i.e., vertically up).

As shown in Figure 5-1, a total of 7 CMOS cameras (4 Photron SA-4, 2 Photron SA-1.1, and 1 Photron SA-6) were used to simultaneously capture the VLIF signal generated. All cameras were aligned in the *x*-*y* plane and their orientations were therefore completely specified by θ, defined as the angle formed by the optical axis of a camera relative to the positive *x* direction. The focal

length and *f*-number of the lenses used on all cameras were 105 mm and 2.8, respectively. Each lens was equipped with a 532 ± 10 nm OD4 notch filter to block any reflection or scattering of the excitation laser. The operation of the cameras and excitation laser was synchronized using control electronics, and the camera control and images acquisition were centralized on a computer. Prior to any measurement, a calibration target was used to determine the orientation and location of the cameras using a view registration program [30] . The orientation of camera 1 through 7 was determined to be θ = 90.0^o, 127.5^o, 213.7^o, 240.2^o, 272.2^o, 316.9^o and 48.9^o, respectively, with an accuracy within ±0.5^o.

Before performing measurements in the target flow, it is also necessary to characterize the profile of the excitation VLIF laser pulses, since the VLIF signal depends on both the I_2 vapor concentration and the laser intensity profile. The characterization of intensity profile of the VLIF laser pulses was accomplished with a help of a static dye cell. We used a cell (with a length and height of 50 mm and a thickness of 0.5 mm) to hold a thin layer of uniform dye solution (with a thickness of 0.5 mm). The solvent was distilled water and the dye was Rhodamine 6G, which can be excited by the 527 nm laser pulses generated by the VLIF laser. The dye cell was then placed in the measurement volume perpendicular to the laser propagation direction and at various *x* locations. At each *x* location, the dye solution was illuminated by the VLIF pulses and emitted LIF photons, which were imaged by a camera along the *x* direction. An example of such image taken at *x* = 25 mm (corresponding to the right surface of the measurement volume) is shown in Figure 5-2(a). Due to the thinness of the dye solution in the cell, the integration effects in the dye were neglected and hence the image shown in Figure 5-2(a) was taken as the 2D intensity profile of the VLIF excitation pulse at *x* = 25 mm. Compiling such 2D profiles at various *x* locations generated a 3D profile of the intensity to be used in the subsequent reconstruction. The pulse-to-pulse

variation of the VLIF laser was measured to be ~3%. Monitoring the pulse profile in situ (with additional cameras) can help to reduce such uncertainty.

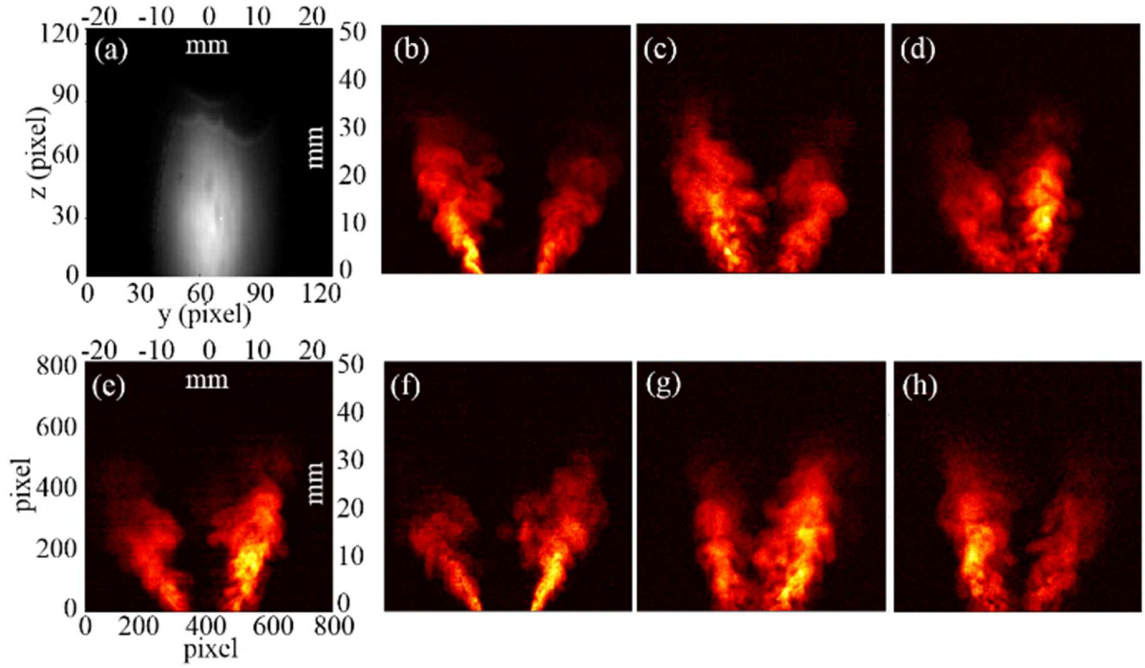

Figure 5-2. Panel (a): 2D spatial profile of the VLIF laser at x = 25 mm. Panels (b) – (f): the VLIF projections captured by camera 1 through 7

Figure 5-2(b) - 2(h) shows a set of example VLIF signals (termed *projections*) captured simultaneously at 5 kHz by camera 1 through 7 using the experimental setup described above. Here the target flow was created by placing a rod with a diameter of 3.18 mm at the exit of the jet (the rod was placed along the y direction as shown in Figure 5-1). The flow was moderately turbulent with a Reynolds number of ~2000 defined based on the jet exit diameter. As seen, the rod created a recognizable V-shaped flow pattern to facilitate the description of the results. For instance, projections captured by camera 1 and 5, which were aligned almost perpendicular to the rod, clearly show the V-shaped flow pattern. These projections were single-shot measurements and all with a pixel resolution of 800 × 800 pixels after cropping (and each pixel corresponded to a physical dimension of ~0.06 mm).

5.3 Tomographic Reconstruction

Different from the reconstruction method used in Chapter 4, a recently developed non-linear reconstruction algorithm is applied here to solve the concentration field more efficiently. The nonlinear algorithm was based on a variation of the Algebraic Reconstruction Technique (ART) algorithm [49, 97]. The major variation involves addressing the absorption of the excitation pulse caused by I_2 [31, 97]. Figure 5-3 schematically shows the formulation of the tomography problem to illustrate this variation. As shown, the 3D distribution of I_2 concentration is denoted as C and discretized into voxels under the Cartesian coordinate system previously defined in Figure 5-1. An imaging system collects the VLIF signal emitted to form a projection P on the camera chip. The projection P depends on two factors: the parameters of the imaging system and the modulation of the signal due to absorption. The parameters of the imaging system include the distance and orientation of the imaging system, specified by r (distance), θ (azimuth angle), and ϕ (inclination angle, zero in this chapter). The effects of all these parameters are reflected in the point spread function (*PSF*) of the imaging system [49, 63]. The modulation of the target signal is caused by the absorption of the excitation laser pulse by I_2 vapor, and such modulation is reflected in a modulation function Γ, an exponentially decaying function in this case following the Beer-Lambert absorption law.

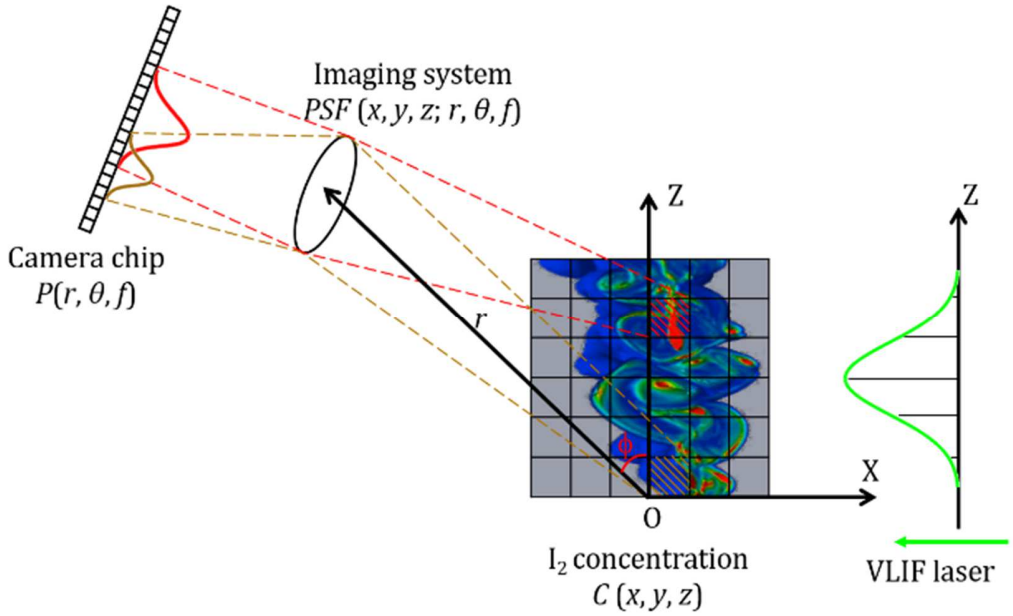

Figure 5-3. Formulation of the VLIF tomography problem.

Considering both the imaging system and the signal modulation due to absorption, the relationship between the measured projection P and C can be mathematically expressed as:

$$\boldsymbol{P} = \boldsymbol{PSF} \cdot \left(\boldsymbol{\Gamma} \circ \boldsymbol{C} \right) \tag{5-1}$$

where $\boldsymbol{P}$ presents the projection vector formed by organizing the measured projections pixel by pixel, $\boldsymbol{PSF}$ the point spread function in matrix form, $\boldsymbol{C}$ the vector formed by organizing the discretized sought property voxel by voxel and lastly $\boldsymbol{\Gamma}$ the attenuation function in matrix form. The operator '$\circ$' represents the Hadamard product and '$\cdot$' matrix and vector product. This chapter uses bold letters to symbolize vectors or matrices formed by discretizing their corresponding continuous functions. The problem is to solve for $\boldsymbol{C}$ with $\boldsymbol{P}$ measured at different locations and orientations, and the problem here is a nonlinear tomography problem due to the nonlinear modulation function Γ. A new algorithm was therefore developed based on the ART algorithm (which is an established algorithm for linear tomography problems) to address the nonlinearity. The new algorithm was code named NIRT (Nonlinear Iterative Reconstruction Technique), and

was detailed and validated in [31]. Briefly, in the NIRT algorithm, a nonlinear point spread function was derived to combine the *PSF* and Γ terms in Eq. (5-1) to allow the development of an iterative scheme. A ray-tracing and Monte-Carlo method were then combined to track the propagation of the excitation pulse and the absorption through the measurement volume [65].

Figure 5-4 shows two sets of results reconstructed by the NIRT algorithm at two different times, t = 0.0 ms and t = 4.0 ms. Figure 5-4(a) shows the 3D reconstruction obtained using the projections shown in Figure 5-2 (which was defined as t = 0.0 ms), and Figure 5-4(b) shows the reconstruction obtained 4.0 ms later. In these reconstructions, the computational domain was set to a volume of 50× 50× 50 mm^3 to encompass the entire flow illuminated. The computational domain was discretized into 128 × 128 × 128 voxels, resulting in nominal spatial resolution of 0.39 mm in all three directions. Figure 5-4(a) and 4(b) show the 3D renderings of the relative I_2 vapor concentration, illustrating the overall V shape of flow as expected.

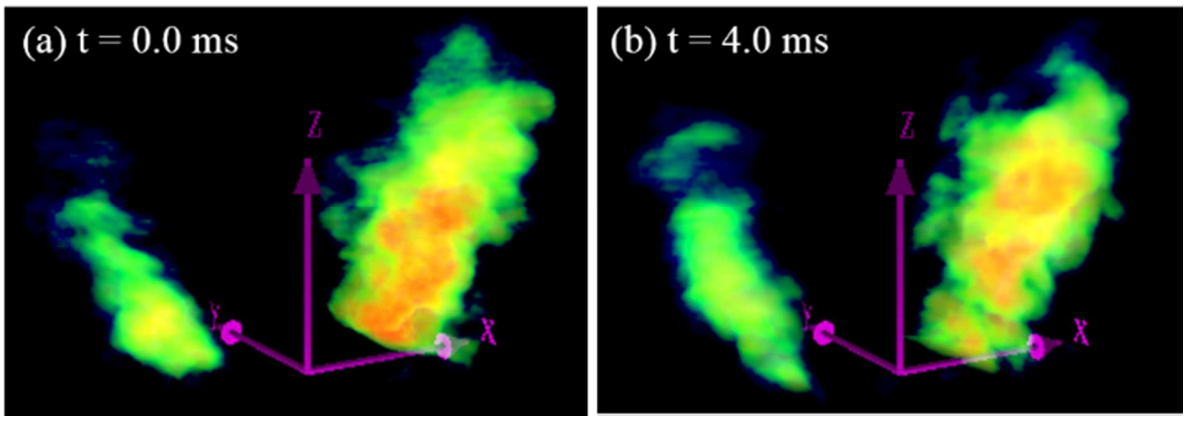

Figure 5-4. 3D rendering of the reconstructed I_2 vapor concentration at t = 0.0 ms and t = 4.0 ms.

To examine the 3D reconstructions more closely, Figure 5-5(a) shows a planar slice taken out the reconstruction at three different times (t = 0.0, 0.2 and 1.0 ms). The slice was at the jet's central plane at $y = 0$ (i.e., the x-z plane at $y = 0$). As a comparison, Figure 5-5(b) shows the line-of-sight integrated VLIF signal measured on camera 1 at the same times. As shown in Figure 5-1, camera

1 was positioned along the *y* direction, and therefore, both Figure 5-5 (a) and 5(b) show the structure of the flow when viewed along the *y* direction. Therefore, both the VLIF and projection measurements captured the same overall flow structure, e.g., the overall V shape of the flow, the taller extend of the left branch than the right, and the higher concentration of I_2 near the bottom of the left branch than the right. However, differences between Figure 5-5(a) and 5(b) are notable because one is a 2D measurement the other line-of-sight integrated. For example, the region with high I_2 concentration near the bottom of the left branch (i.e., the region highlighted in the oval) appeared to be larger in Figure 5-5(b) than 5(a) because Figure 5-5(b) was line-of-sight integrated while Figure 5-5(a) was not.

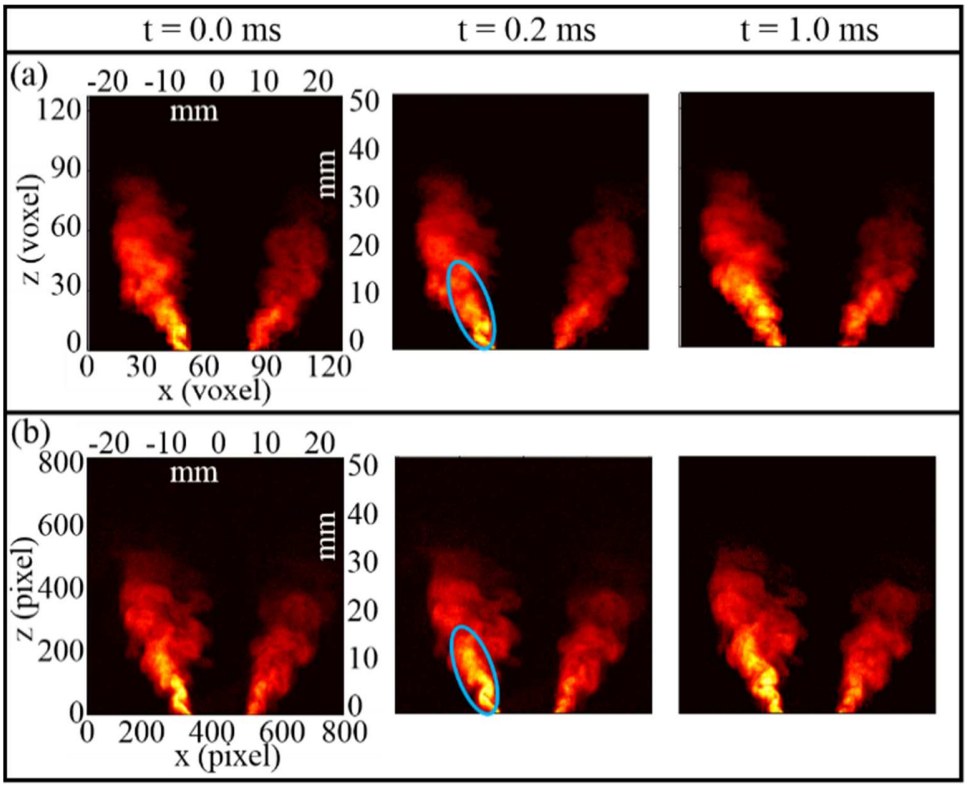

Figure 5-5. Comparison of the central slices taken out of the reconstruction (panel (a)) and the VLIF projections measured by camera 1 (panel (b)) at different times.

Temporally, as seen from Figure 5-5 (both from the VLIF and projection measurements), the 5 kHz repletion rate was sufficient to resolve the dynamics of the flow. The results obtained at t =

0.0 ms and 0.2 ms are visually identical as shown (upon closer examination, the results shown in Figure 5-5(a) at t = 0.0 and 0.2 ms were different by an offset within 1 voxel, i.e., 0.39 mm). In contrast, the results at t = 0.0 ms and 1.0 ms are visually different as seen from Figure 5-5 (again, both from the VLIF and the projection measurements, showing that a repetition rate of 1 kHz was not sufficient to capture the temporal dynamics of this flow).

5.4 VLIF Measurement at Multiple Repetition Rates

To further illustrate the capabilities and limitations of VLIF, measurements were taken under different conditions in terms of repetition frequencies and excitation pulse energy. The focus is to understand the signal level of VLIF measurements and its impact on the reconstruction accuracy.

Using the experimental setup described in Section 2, VLIF measurements were performed with a repetition frequency ranging from 1 to 10 kHz, and Figure 5-6 shows the pulse duration and pulse energy as a function of the repetition frequency. As seen, the pulse duration increased from ~150 ns to ~425 ns and the pulse energy decreased from ~72 mJ to ~15 mJ in this range (though the laser profile remained stable as that shown in Figure 5-2(a)).

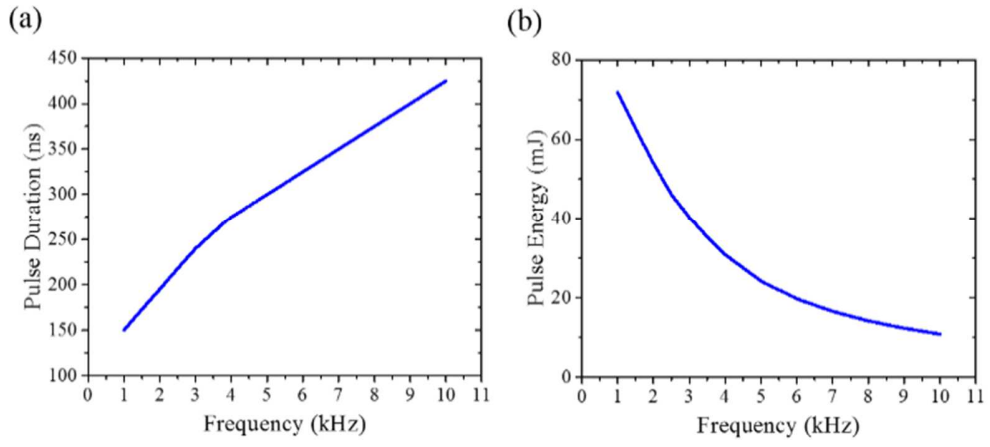

Figure 5-6. Pulse duration and energy of excitation laser pulse as a function of repetition frequency.

A two-level LIF model [1, 98] was adapted to analyze the signal. The number of LIF photons received by a pixel on a camera from a small probe region in the measurement volume is expressed as follows:

$$N_{LIF} = C \cdot \frac{\Omega}{4\pi} \cdot \frac{B_{12}}{B_{12} + B_{21}} \cdot \frac{A_{21}}{1 + \frac{(A_{21} + Q_{21})c}{(B_{12} + B_{21})I_\nu}} \cdot \Delta t \cdot \Delta V \tag{5-2}$$

where Ω is the collection angle of the pixel relative to probe region; B_{12}, B_{21} and A_{21} are the Einstein coefficients; Q_{21} the quenching rate coefficient; I_ν the spectral irradiance of the excitation laser; c the speed of light; Δt the laser pulse duration; and ΔV the volume of the probed region. In this chapter, the Einstein coefficients were taken from [99] and listed in Table 1. Among all the possible quenching mechanisms, only the collisional quenching Q_{21} is considered because it is dominant over the pre-dissociation effect at atmospheric pressure, and the value used in this chapter is also listed in Table 1 [61, 100]. With the pulse duration and pulse energy plotted in Figure 5-6 and the laser profile measured in Figure 5-2(a), the spectral irradiance was calculated and listed in Table 1.

Table 5-1. LIF related parameters

Einstein A coefficient A_{21} (s^{-1})	9.35×10^5
Einstein B coefficient B_{21} ($J^{-1}m^3sec^{-2}$)	9.85×10^{18}
Einstein B coefficient B_{12} ($J^{-1}m^3sec^{-2}$)	9.85×10^{18}
Quenching coefficient Q (sec^{-1})	3.80×10^8
Laser repetition rate f (kHz)	1 ~ 10
Laser pulse duration Δt (ns)	150 ~ 420
Laser spectral irradiance Iv ($Jm^{-2}Hz^{-1}sec^{-1}$)	$4.4 \times 10^{-4} \sim 1.0 \times 10^{-2}$

With the above parameters, Figure 5-7 shows the VLIF signal level of camera 1 computed based on Eq. (5-2) at different repetition frequencies. The results for other cameras show similar trend as that shown here. The computation was processed in three steps. First, a phantom distribution of I_2 concentration (i.e., C) was created based on simulation. To facilitate the comparison between the computational and experimental results, the phantom was created to replicate the concentration distribution experimentally measured (i.e., similar to that shown in Figure 5-4(a)). The phantom was discretized into voxels as described earlier. Second, for each pixel on the camera, the collection angle Ω corresponding to different voxels in the phantom was calculated using the Monte Carlo and ray tracing method mentioned in Section 3. With Ω and the other parameters as shown in Table 5-1, the number of LIF photons received on every pixel emitted from every voxel (i.e., N_{LIF}) on a single can be calculated according to Eq. (5-2). Then the contributions emitted from all voxels were calculated and integrated to obtain the projection on the camera. Third, the projection obtained in step 2 was integrated pixel-by-pixel and the integrated signal was used to represent the overall signal level of the VLIF measurements.

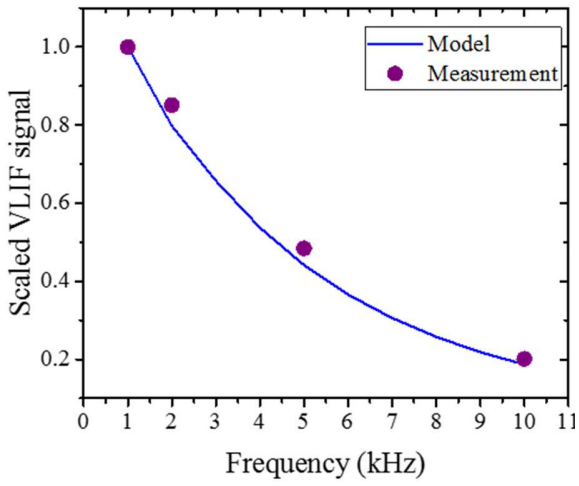

Figure 5-7. Simulated and measured VLIF signal level at different repetition rates.

Figure 5-7 shows the overall signal level obtained from the computation described and that obtained by experimentally measured projections. All the experimental results were scaled by a common factor to account practical scaling factors that were not considered in the model (such as the conversion factor from optical to electrical signal in the camera, or the reflection losses at the surfaces of optical components). The fact that a common scaling factor can collapse all the experimental data to close agreement with the computations supports that the model captured the major physics of the VLIF measurements. As Figure 5-7 shows, the VLIF signal level decreases significantly with increasing repetition rate. Both the computational and experimental results show that the VLIF signal level decreased by a factor of ~5× when the repetition rate increased from 1 to 10 kHz. Such decrease was primarily due to the longer pulse duration and lower pulse energy (resulting in lower irradiance) of the laser as its repetition rate increases.

With the ability to accurately simulate the VLIF signal level, the relationship between measurement repetition rate and 3D measurement accuracy can be studied. Assuming shot-limited detection, the uncertainty in the projections is determined by the signal level shown in Figure 5-7, which then can be incorporated into the reconstruction algorithm to study the reconstruction accuracy. More specifically, an uncertainty was estimated based on the overall signal level, and artificial noise (following a Gaussian distribution with the estimated uncertainty as mean) was added to projections. The artificially contaminated projections were used as inputs the tomographic algorithm to obtain a reconstruction, and the reconstruction error (E_R) can be now quantified as:

$$E_R = \frac{\sum_{n=1}^{N} \left| C_n^{rec} - C_n^{true} \right|}{C_n^{true}} \tag{5-3}$$

where N is the total number of voxels used in the reconstruction, n the index of voxels, C_n^{rec} and C_n^{true} the reconstructed and phantom distribution at the n^{th} voxel, respectively.

Figure 5-8 shows the results of E_R obtained at different repetition rates. As seen, the reconstruction error increases the measurement repetition rate increase, due to the increasing lower signal level and higher uncertainty in the VLIF projections. At a repetition rate of 1 kHz, an E_R near 2% can be obtained, in contrast to ~12% at a repetition at 10 kHz as suggested by these results. Based on these results, the reconstructions shown in Figure 5-4 obtained at 5 kHz was accurate within ~5%. Admittedly, such accuracy was obtained under the assumption of shot-limited detection, and the actual accuracy will be worse than this because of other sources of experimental uncertainty. The results shown here are valuable as they illustrate the limit of the performance of VLIF measurements under high repetition rates, and also the potential improvement in reconstruction accuracy that can be achieved with enhanced signal level (e.g., by using more powerful lasers or imaging systems with better collection efficiency).

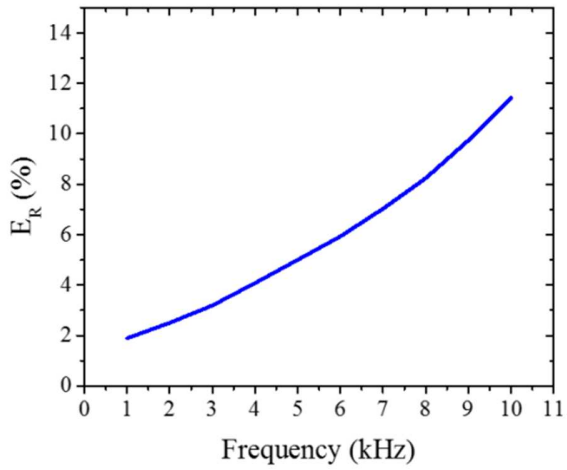

Figure 5-8. Reconstruction accuracy of I_2 jet flow calculated at different repetition rates.

5.5 Summary

In summary, this chapter demonstrated 4D imaging measurements (made in a duration between 150 to 450 ns) in turbulent flows at repetition rates up to 10 kHz, and performed accompanying analysis to illustrate the capabilities and limitations of high speed 4D measurements. The 4D

measurements were demonstrated in a 50 × 50 × 50 mm^3 volume with a total of 128 × 128 × 128 voxels using a technique termed VLIF (volumetric laser induced fluorescence). The VLIF technique excited the seeded I_2 vapor volumetrically, and the volumetric LIF signals emitted were then simultaneously collected by multiple cameras from different orientations. Based on the projections measured by these cameras, tomographic reconstruction was performed to obtain 4D measurements. To study the capabilities and limitations of VLIF, the experimental data were analyzed to elucidate the relationship among the VLIF signal level, reconstruction accuracy, repetition rate, excitation pulse energy, and pulse duration. These results suggest that the overall VLIF signal level decreases significantly with increasing repetition rate due to the decreasing pulse energy and increasing pulse duration, both characteristics typical to high repetition rate Nd: YLF and Nd: YAG lasers. As a result of the decreasing signal level, the reconstruction accuracy decreases. With the status of the experiments demonstrated in this chapter, the overall 3D reconstruction error was estimated to be ~2% at a repetition rate of 1 kHz and ~12% at a repetition rate of 10 kHz.

Chapter 6 Conclusion and Future Work

This dissertation described the development, validation, and application of two novel optical diagnostic approaches, namely Tomographic Chemiluminesence (TC) and Volumetric Laser Induced Fluorescence (VLIF), for 4D measurements in turbulent flows and flames. Both techniques use advanced tomographic algorithms, such as Algebraic Reconstruction Technique (ART) and Nonlinear Iterative Reconstruction Technique (NIRT), to reconstruct 4D measurements of key flame and flow properties, such as flame front location, flame front curvature, chemical species concentrations, etc. Both techniques have been numerically verified using phantom study and experimentally validated by performing both qualitative and quantitative comparison against established diagnostic technique such as Planar Laser Induced Fluorescence (PLIF). After the validation of both techniques, their practical applications in highly turbulent combustion and non-reacting flows have then been demonstrated. The results show that these methods have great potential to fully resolve complicated flows and flames with high spatiotemporal resolution.

Based on the lessons learned in this work, the following research directions are suggested for future investigation:

1) As an extension of VLIF measurements in non-reactive flow (e.g. a turbulent jet flow seeded with iodine), application of VLIF measurements on reactive flows should be explored and investigated. The measurements will be single-shot measurements similar to the measurements in non-reactive flows, and CH radical is a promising species for such measurements. The VLIF measurements can be experimentally validation again by comparing the VLIF against PLIF measurements based on CH. Both experimental demonstration and validation measurements should be performed on both laminar and

turbulent flames. A focus in these measurements is to examine if the VLIF technique can maintain the same level of capability in resolving the 3D spatial structures of reactive flows comparing with that in non-reactive flows.

2) Besides the experimental demonstrations discussed in this work, a thorough parametric study is needed to help us understand the intrinsic mechanism of VLIF. Compared to traditional planar techniques, it is not straightforward to understand the VLIF approach for several reasons. First, the VLIF technique has an additional dimension – the depth of the field of view compared to the PLIF measurements. The VLIF approach illuminates the field of view volumetrically, and as a result, the LIF signals captured by the cameras are line-of-sight integration from the entire 3D field of view, fundamentally different from the signals generated in PLIF or scanning PLIF measurements. Second, the VLIF technique involves a tomographic inversion using the measured projections as inputs to reconstruct the final 3D measurements. The accuracy and spatial resolution of the reconstruction depend on the 3D field of view and the signal level of the projections, and the dependence is different from that of in the PLIF or scanning PLIF method. Therefore, the goal of the parametric study is to investigate the performance metrics of the VLIF technique and map out their relationships.

3) Extend the TC and VLIF concept to the volumetric measurements of other properties, such as flow velocity and temperature. Take 4D velocity measurement as an example. First developed by Elsinga[101], the tomo-PIV is utilized to reconstruct the velocity field of flows based on line-of-sight projections and has been applied in numerous kinds of flow and combustion systems[102-104]. Some the ideas used in the reconstruction algorithm and validation of TC and VLIF can be applied for tomo-PIV. For example, an experiment

can be designed to directly compare 3D tomo-PIV measurements against established planar PIV measurements, or using controlled cell measurements. A controlled cell can be designed to be embedded with tracer particles, then cell then can be moved translationally and/or rotated and the movement of the embedded particles will create precisely controlled movement to create phantom velocity distributions for validating tomo-PIV. This approach will provide experimental data to perform a direct comparison between the measured and exact velocity field vectors by vectors, and therefore is worth pursing as a future research direction.

Reference

1. Eckbreth, A.C., *Laser diagnostics for combustion temperature and species*. Gordon and Breach Publishers. Vol. 3. 1996: CRC press.
2. Floyd, J. and A.M. Kempf, *Computed Tomography of Chemiluminescence (CTC): High resolution and instantaneous 3-D measurements of a Matrix burner*. Proc. Combust. Inst., 2011. **33**(1): p. 751-758.
3. Dalzell, W. and A. Sarofim, *Optical constants of soot and their application to heat-flux calculations.* J. of Heat Trans., 1969. **91**(1): p. 100-104.
4. De Iuliis, S., et al., *Determination of the soot volume fraction in an ethylene diffusion flame by multiwavelength analysis of soot radiation.* Combust. Flame, 1998. **115**(1): p. 253-261.
5. Arola, A., et al., *A case study on biomass burning aerosols: effects on aerosol optical properties and surface radiation levels.* Atmo. Chem. Phy., 2007. **7**(16): p. 4257-4266.
6. Zembrod, A., H. Puell, and J. Giordmaine, *Surface radiation from non-linear optical polarisation.* Opt. and Quant. Electr., 1969. **1**(1): p. 64-66.
7. Adrian, R.J. and J. Westerweel, *Particle image velocimetry*2011: Cambridge University Press.
8. Scarano, F., *Tomographic PIV: principles and practice.* Meas. Sci. Tech., 2013. **24**(1): p. 012001.
9. Abbiss, J., T. Chubb, and E. Pike, *Laser Doppler anemometry.* Opt. & Laser Tech., 1974. **6**(6): p. 249-261.
10. Durst, F., A. Melling, and J.H. Whitelaw, *Principles and practice of laser-Doppler anemometry.* NASA STI/Recon Technical Report A, 1976. **76**: p. 47019.
11. Qiu, H.-H. and M. Sommerfeld, *A reliable method for determining the measurement volume size and particle mass fluxes using phase-Doppler anemometry.* Exp. Fluids, 1992. **13**(6): p. 393-404.
12. Sommerfeld, M. and H.-H. Qiu, *Characterization of particle-laden, confined swirling flows by phase-doppler anemometry and numerical calculation.* Inter. J of multi. flow, 1993. **19**(6): p. 1093-1127.
13. Kinsey, J.L., *Laser-induced fluorescence.* Annual Rev. of Phys.Chemi., 1977. **28**(1): p. 349-372.
14. Dyer, M.J. and D.R. Crosley, *Two-dimensional imaging of OH laser-induced fluorescence in a flame.* Opt. Lett., 1982. **7**(8): p. 382-384.
15. Lozano, A., B. Yip, and R.K. Hanson, *Acetone: a tracer for concentration measurements in gaseous flows by planar laser-induced fluorescence.* Exp. Fluids, 1992. **13**(6): p. 369-376.
16. Shaddix, C.R. and K.C. Smyth, *Laser-induced incandescence measurements of soot production in steady and flickering methane, propane, and ethylene diffusion flames.* Combust. Flame, 1996. **107**(4): p. 418-452.

17. Santoro, R.J. and C.R. Shaddix, *Laser-induced incandescence.* Appl. Combust. Diag., 2002: p. 252-286.

18. Kneipp, K., et al., *Single molecule detection using surface-enhanced Raman scattering (SERS).* Phys. Rev. Lett., 1997. **78**(9): p. 1667.

19. Nie, S. and S.R. Emory, *Probing single molecules and single nanoparticles by surface-enhanced Raman scattering.* Sci., 1997. **275**(5303): p. 1102-1106.

20. Clays, K. and A. Persoons, *Hyper-Rayleigh scattering in solution.* Phys. Rev. Lett., 1991. **66**(23): p. 2980.

21. Inouye, S., et al., *Superradiant Rayleigh scattering from a Bose-Einstein condensate.* Sci., 1999. **285**(5427): p. 571-574.

22. Lei, Q., et al., *Analysis of four-dimensional Mie imaging using fiber-based endoscopes.* Appl. Opt., 2014. **53**(28): p. 6389-6398.

23. Wiscombe, W.J., *Improved Mie scattering algorithms.* Appl. Opt., 1980. **19**(9): p. 1505-1509.

24. Schiff, H., G. Mackay, and J. Bechara, *The use of tunable diode laser absorption spectroscopy for atmospheric measurements.* Research on chemi. interm., 1994. **20**(3-5): p. 525-556.

25. Faber, D.J., et al., *Light absorption of (oxy-) hemoglobin assessed by spectroscopic optical coherence tomography.* Opt. Lett., 2003. **28**(16): p. 1436-1438.

26. Wright, P., et al., *High-speed chemical species tomography in a multi-cylinder automotive engine.* Chemi. Eng. J., 2010. **158**(1): p. 2-10.

27. Hossain, M.M.M., G. Lu, and Y. Yan, *Optical fiber imaging based tomographic reconstruction of burner flames.* IEEE Trans. on Instr. and Meas., 2012. **61**(5): p. 1417-1425.

28. Kang, M., X. Li, and L. Ma. *Calibration of Fiber Bundles for Flow and Combustion Measurements.* in *AIAA Paper (2014-0397)*. 2014. National Harbor, MD.

29. Yong, Y., et al., *Recent advances in flame tomography.* Chinese Journal of Chemical Engineering, 2012. **20**(2): p. 389-399.

30. Kang, M., Y. Wu, and L. Ma, *Fiber-based endoscopes for 3D combustion measurements: view registration and spatial resolution.* Combust. Flame, 2014. **161**(12): p. 3063-3072.

31. Lei, Q., et al., *Development and validation of a reconstruction algorithm for three-dimensional nonlinear tomography problems.* Opt. Expr., 2016. **24**(14): p. 15912-15926.

32. Cai, W. and L. Ma, *Applications of Critical Temperature in Minimizing Functions of Continuous Variables With Simulated Annealing Algorithm.* Comp. Phys. Comm., 2010. **181**(1): p. 11-16.

33. Fincham, A. and G. Delerce, *Advanced optimization of correlation imaging velocimetry algorithms.* Exp. Fluids, 2000. **29**(1): p. S013-S022.

34. Ma, L., et al., *Comparison of 2D and 3D flame topography measured by planar laser-induced fluorescence and tomographic chemiluminescence.* Appl. Opt., 2016. **55**(20): p. 5310-5315.

35. Wellander, R., M. Richter, and M. Alden, *Time resolved, 3D imaging (4D) of two phase flow at a repetition rate of 1 kHz.* Opt. Expr., 2011. **19**(22): p. 21508-21514.

36. Yip, B., R.L. Schmitt, and M.B. Long, *Instantaneous three-dimensional concentration measurements in turbulent jets and flames.* Opt. Lett., 1988. **13**(2): p. 96-98.

37. Floyd, J., P. Geipel, and A.M. Kempf, *Computed Tomography of Chemiluminescence (CTC): Instantaneous 3D measurements and Phantom studies of a turbulent opposed jet flame.* Combust. Flame, 2011. **158**(2): p. 376-391.

38. Li, X. and L. Ma, *Volumetric imaging of turbulent reactive flows at kHz based on computed tomography.* Opt. Expr., 2014. **22**(4): p. 4768-4778.

39. Kychakoff, G., et al., *Movies and 3-D images of flowfields using planar laser-induced fluorescence.* Appl. Opt., 1987. **26**(13): p. 2498-2500.

40. Nygren, J., et al., *Three-dimensional laser induced fluorescence of fuel distributions in an HCCI engine.* Proc. Combust. Inst., 2002. **29**(1): p. 679-685.

41. Hult, J., et al., *Quantitative three-dimensional imaging of soot volume fraction in turbulent non-premixed flames.* Exp. Fluids, 2002. **33**(2): p. 265-269.

42. Lackner, M., *Tunable diode laser absorption spectroscopy (TDLAS) in the process industries–a review.* Rev. in Chemi. Eng., 2007. **23**(2): p. 65-147.

43. Werle, P., R. Mücke, and F. Slemr, *The limits of signal averaging in atmospheric trace-gas monitoring by tunable diode-laser absorption spectroscopy (TDLAS).* Appl. Phys. B, 1993. **57**(2): p. 131-139.

44. Ma, L. and W. Cai, *Determination of the Optimal Regularization Parameters in Hyperspectral Tomography.* Appl. Opt., 2008. **47**(23): p. 4186-4192.

45. Ma, L., et al., *Tomographic imaging of temperature and chemical species based on hyperspectral absorption spectroscopy.* Opt. Expr., 2009. **17**(10): p. 8602-8613.

46. Wu, Y., Q. Lei, and L. Ma, *Experimental demonstration of 4D imaging in two-phase flows based on computed tomography at 5 kHz.* Appl. Opt., 2014. **53**(24): p. 5547-5553.

47. Cai, W., et al., *Numerical and experimental validation of a three-dimensional combustion diagnostic based on tomographic chemiluminescence.* Opt. Expr., 2013. **21**(6): p. 7050-7064.

48. Li, X. and L. Ma, *Capabilities and limitations of 3D flame measurements based on computed tomography of chemiluminescence.* Combust. Flame, 2015. **162**(3): p. 642-651.

49. Cai, W., X. Li, and L. Ma, *Practical aspects of implementing three-dimensional tomography inversion for volumetric flame imaging.* Appl. Opt., 2013. **52**(33): p. 8106-8116.

50. Strner, S., et al. *Joint planar CH and OH LIF imaging in piloted turbulent jet diffusion flames near extinction*. in *Symposium (International) on Combustion*. 1992. Elsevier.

51. Driscoll, J.F., *Turbulent premixed combustion: Flamelet structure and its effect on turbulent burning velocities.* Prog. Energy Combust. Sci., 2008. **34**(1): p. 91-134.

52. Filatyev, S.A., et al., *Measured properties of turbulent premixed flames for model assessment, including burning velocities, stretch rates, and surface densities.* Combust. Flame, 2005. **141**(1-2): p. 1-21.

53. Rao, X., et al., *Combustion dynamics of plasma-enhanced premixed and nonpremixed flames.* Plasma Sci., IEEE Transactions on, 2010. **38**(12): p. 3265-3271.

54. Hammack, S.D., et al., *High-repetition-rate OH planar laser-induced fluorescence of a cavity flameholder*. J. of Prop. and Pow., 2013. **29**(5): p. 1248-1251.

55. Carter, C.D., J.M. Donbar, and J.F. Driscoll, *Simultaneous CH planar laser-induced fluorescence and particle imaging velocimetry in turbulent nonpremixed flames.* Appl. Phys. B, 1998. **66**(1): p. 129-132.

56. Zhang, M., et al., *Estimation of 3D flame surface density and global fuel consumption rate from 2D PLIF images of turbulent premixed flame.* Combust. Flame, 2015. **162**(5): p. 2087-2097.

57. Steinberg, A.M. and J.F. Driscoll, *Straining and wrinkling processes during turbulence–premixed flame interaction measured using temporally-resolved diagnostics.* Combust. Flame, 2009. **156**(12): p. 2285-2306.

58. Steinberg, A.M. and J.F. Driscoll, *Stretch-rate relationships for turbulent premixed combustion LES subgrid models measured using temporally resolved diagnostics.* Combust. Flame, 2010. **157**(7): p. 1422-1435.

59. Steinberg, A.M., J.F. Driscoll, and S.L. Ceccio, *Measurements of turbulent premixed flame dynamics using cinema stereoscopic PIV.* Exp. Fluids, 2008. **44**(6): p. 985-999.

60. Donbar, J.M., J.F. Driscoll, and C.D. Carter, *Strain rates measured along the wrinkled flame contour within turbulent non-premixed jet flames.* Combust. Flame, 2001. **125**(4): p. 1239-1257.

61. Carter, C.D., S. Hammack, and T. Lee, *High-speed planar laser-induced fluorescence of the CH radical using the $C^2\sum^+$-X^2(0, 0) band.* Appl. Phys. B, 2014. **116**(3): p. 515-519.

62. Kang, M., X. Li, and L. Ma, *Three-dimensional flame measurements using fiber-based endoscopes.* Proc. Combust. Inst., 2015. **35**(3): p. 3821-3828.

63. DiMarzio, C.A., *Optics for Engineers*2011, Boca Raton, FL: CRC Press Taylor & Francis Group.

64. Cai, W. and L. Ma, *Improved Monte Carlo Model for Multiple Scattering Calculations.* Chin. Opt. Lett., 2012. **10**(1): p. 012901.

65. Zhao, Y., X. Li, and L. Ma, *Multidimensional Monte Carlo Model for Two-photon Laser-induced Fluorescence and Amplified Spontaneous Emission.* Comp. Phys. Comm., 2012. **183**(8): p. 1588-1595.

66. Li, X. and L. Ma, *Effects of Line-narrowing of Amplified Spontaneous Emission Analyzed by a Monte Carlo Model.* J. Quan. Spec. Radi. Trans., 2012. **114**: p. 157-166.

67. Kheirkhah, S. and Ö. Gülder, *Turbulent premixed combustion in V-shaped flames: Characteristics of flame front.* Phys. of Flu. , 2013. **25**(5): p. 055107.

68. Sengupta, T.K., *Fundamentals of computational fluid dynamics*. Vol. 364. 2004: Universities Press Hyderabad (India).

69. O'neill, B., *Elementary differential geometry*2006: Academic press.

70. Kühnel, W., *Differential geometry: curves-surfaces-manifolds*. Vol. 16. 2006: American Mathematical Society.

71. Kerl, J., C. Lawn, and F. Beyrau, *Three-dimensional flame displacement speed and flame front curvature measurements using quad-plane PIV.* Combust. Flame, 2013. **160**(12): p. 2757-2769.

72. Cant, S., *RANS and LES Modelling of Premixed Turbulent Combustion*. Turbulent Combustion Modeling: Advances, New Trends and Perspectives, ed. T. Echekki and E. Mastorakos. Vol. 95. 2011: Springer Science & Business Media. 63-90.

73. Echekki, T. and E. Mastorakos, *Turbulent Combustion: Concepts, Governing Equations and Modeling Strategies*. Turbulent Combustion Modeling: Advances, New Trends and Perspectives, ed. T. Echekki and E. Mastorakos. Vol. 95. 2011: Springer Netherlands. 19-39.

74. Pope, S.B., *Small scales, many species and the manifold challenges of turbulent combustion.* Proc. Combust. Inst., 2013. **34**: p. 1-31.

75. Clavin, P., *Dynamic behavior of premixed flame fronts in laminar and turbulent flows.* Prog. Energy Combust. Sci., 1985. **11**(1): p. 1-59.

76. Gülder, Ö.L. *Turbulent premixed flame propagation models for different combustion regimes*. in *Symp. (Int.) Combust.* 1991. Elsevier.

77. Bell, J.B., et al., *Numerical simulation of a laboratory-scale turbulent V-flame.* Proc. National Acade. Sci. U.S.A, 2005. **102**(29): p. 10006-10011.

78. Candel, S., et al., *Advances in combustion and propulsion applications.* Euro. Jour. Mech. B-Fluids, 2013. **40**: p. 87-106.

79. Fiorina, B., D. Veynante, and S. Candel, *Modeling Combustion Chemistry in Large Eddy Simulation of Turbulent Flames.* Flow Turbu. Combust., 2015. **94**(1): p. 3-42.

80. Miller, V.A., V.A. Troutman, and R.K. Hanson, *Near-kHz 3D tracer-based LIF imaging of a co-flow jet using toluene.* Meas. Sci. Tech., 2014. **25**(7): p. 075403.

81. Wellander, R., M. Richter, and M. Alden, *Time-resolved (kHz) 3D imaging of OH PLIF in a flame.* Exp. Fluids, 2014. **55**(6): p. 1-12.

82. Cho, K.Y., et al., *High-repetition-rate three-dimensional OH imaging using scanned planar laser-induced fluorescence system for multiphase combustion.* Appl. Opt., 2014. **53**(3): p. 316-326.

83. Ma, L., et al., *50-kHz-rate 2D Imaging of Temperature and H2O Concentration at the Exhaust Plane of a J85 Engine using Hyperspectral Tomography.* Opt. Expr., 2013. **21**(1): p. 1152-1162.

84. Ma, L., et al., *Tomographic Imaging of Temperature and Chemical Species Based on Hyperspectral Absorption Spectroscopy.* Opt. Express, 2009. **17**(10): p. 8602-8613.

85. Ma, L., et al., *3D measurements of ignition processes at 20 kHz in a supersonic combustor.* Appl. Phys. B, 2015. **119**(2): p. 313-318.

86. Alden, M., et al., *Visualization and understanding of combustion processes using spatially and temporally resolved laser diagnostic techniques.* Proc. Combust. Inst., 2011. **33**: p. 69-97.

87. Cai, W. and L. Ma, *Hyperspectral Tomography Based on Proper Orthogonal Decomposition as Motivated by Imaging Diagnostics of Unsteady Reactive Flows.* Appl. Opt., 2010. **49**(4): p. 601-610.

88. Ushakov, N., *Density of a probability distribution*2001: Springer.

89. Spivak, M., *A comprehensive introduction to differential geometry*. Bull. Amer. Math. Soc. , 1973. **79**: p. 303-306

90. Hanson, R.K., J.M. Seitzman, and P.H. Paul, *Planar laser-fluorescence imaging of combustion gases.* Appl. Phys. B, 1990. **50**(6): p. 441-454.

91. van Cruyningen, I., A. Lozano, and R.K. Hanson, *Quantitative imaging of concentration by planar laser-induced fluorescence.* Exp. Fluids, 1990. **10**(1): p. 41-49.

92. Medford, T., et al. *Stereoscopic Planar Laser-Induced Fluorescence Imaging at 500 kHz*. in *49th AIAA Aerospace Sciences Meeting including the New Horizons Forum and Aerospace Exposition*. 2011. Orlando, FL.

93. Seitzman, J.M., G. Kychakoff, and R.K. Hanson, *Instantaneous temperature field measurements using planar laser-induced fluorescence.* Opt. Lett., 1985. **10**(9): p. 439-441.

94. Zhao, Y., C. Tong, and L. Ma, *Demonstration of a new laser diagnostic based on photodissociation spectroscopy for imaging mixture fraction in a non-premixed jet flame.* Appl. Spectr., 2010. **64**(4): p. 377-383.

95. Zhao, Y., C. Tong, and L. Ma, *Assessment of a Novel Flow Visualization Technique Using Photodissociation Spectroscopy.* Appl. Spectr., 2009. **63**(2): p. 199-206.

96. Zhao, Y., C. Tong, and L. Ma, *Kinetics of I2 and HI photodissociation with implications in flame diagnostics.* Appl. Phys. B, 2011. **104**(3): p. 689-698.

97. Wu, Y., et al., *Single-shot volumetric laser induced fluorescence (VLIF) measurements in turbulent flows seeded with iodine.* Opt. Expr., 2015. **23**(26): p. 33408-33418.

98. Hiller, B. and R. Hanson, *Properties of the iodine molecule relevant to laser-induced fluorescence experiments in gas flows.* Exp. Fluids, 1990. **10**(1): p. 1-11.

99. Capelle, G.A. and H. Broida, *Lifetimes and quenching cross sections of I^2 ($B^3\Pi_{Ou}^+$).* The J. of Chemi. Phys., 1973. **58**(10): p. 4212-4222.

100. Jeffries, J.B., R.A. Copeland, and D.R. Crosley, *Transition probabilities in the $C^2\sum^+$-X^2 II system of CH.* J. of Quant. Spectr. and Rad. Trans., 1987. **37**(5): p. 419-423.

101. Elsinga, G.E., et al., *Tomographic particle image velocimetry*. Exp. Fluids, 2006. **41**(6): p. 933-947.

102. Tokgoz, S., et al., *Spatial resolution and dissipation rate estimation in Taylor--Couette flow for tomographic PIV*. Exp. Fluids, 2012. **53**(3): p. 561-583.

103. Thomas, L., et al. *Influence of geometric parameters and image preprocessing on tomo-PIV results*. in *15th international symposium on applications of laser techniques to fluid mechanics*. 2010.

104. Weinkauff, J., et al., *Tomographic PIV measurements in a turbulent lifted jet flame.* Exp. Fluids, 2013. **54**(12): p. 1-5.